

**1 Deoxygenation and its drivers analyzed in steady state  
2 for perpetually slower and warmer oceans**

**3 Benoît Pasquier<sup>1</sup>, Mark Holzer<sup>1</sup>,**

**4 Matthew A. Chamberlain<sup>2</sup>, Richard J. Matear<sup>2</sup>,**

**5 and Nathaniel L. Bindoff<sup>3</sup>**

**6** <sup>1</sup>School of Mathematics and Statistics, University of New South Wales, Sydney, NSW, Australia

**7** <sup>2</sup>Commonwealth Scientific and Industrial Research Organisation, Hobart, TAS, Australia

**8** <sup>3</sup>Australian Antarctic Program Partnership, Institute for Marine and Antarctic Studies, University of

**9 Tasmania, Hobart, TAS, Australia**

**10 Key Points:**

- 11** • Key drivers of deoxygenation are quantified for oxygen cycles idealized by being  
in equilibrium with perpetually slower oceans
- 12** • Widespread intense abyssal ocean deoxygenation is driven predominantly by slower  
circulations allowing respiration to act over longer times
- 13** • Most of the reduction in preformed oxygen is driven by changes in ventilation pat-  
terns and not by warming-driven reduced solubility

---

Corresponding author: Benoît Pasquier, [b.pasquier@unsw.edu.au](mailto:b.pasquier@unsw.edu.au)

Corresponding author: Mark Holzer, [mholzer@unsw.edu.au](mailto:mholzer@unsw.edu.au)

17      **Abstract**

18      Ocean deoxygenation is an important consequence of climate change that poses an im-  
19      minent threat to marine life and global food security. However, our understanding of the  
20      complex interactions between changes in circulation, solubility, and respiration that drive  
21      global-scale deoxygenation is incomplete. Here, we consider idealized biogeochemical steady  
22      states in equilibrium with perpetually slower and warmer oceans constructed from climate-  
23      model simulations of the 2090s that we hold constant in time. In contrast to simulations  
24      of the end-of-century transient state, our idealized states are intensely deoxygenated in  
25      the abyss, consistent with perpetually reduced ventilation and throttled Antarctic Bot-  
26      tom Water formation. We disentangle the effects of the deoxygenation drivers on pre-  
27      formed oxygen and true oxygen utilization (TOU) using the novel concept of upstream  
28      exposure time, which precisely connects TOU to oxygen utilization rates and preformed  
29      oxygen to ventilation. For our idealized steady states, deoxygenation below 2000 m depth  
30      is due to increased TOU, driven dominantly by slower circulations that allow respi-  
31      ration to act roughly 2–3 times longer thereby overwhelming the effects of reduced respi-  
32      ration rates. Above 500 m depth, decreased respiration and slower circulation closely com-  
33      pensate, resulting in little expansion of upper-ocean hypoxia. The bulk of preformed oxy-  
34      gen loss is driven by ventilation shifting equatorward to where warmer surface waters  
35      hold less oxygen. Warming-driven declines in solubility account for less than 10 % of the  
36      total oxygen loss. Although idealized, our analysis suggests that long-term changes in  
37      the marine oxygen cycle could be driven dominantly by changes in circulation rather than  
38      by thermodynamics or biology.

39      **Plain Language Summary**

40      Climate change is driving oxygen out of the ocean, threatening marine life and global  
41      food security. However, the precise contributions of the chemical, physical, and biolog-  
42      ical processes that control oxygen levels are not well known because of their complex in-  
43      teractions. To better understand these interactions, we consider idealized simulations  
44      of a global oxygen cycle that is fully equilibrated with a perpetually warmer and slower  
45      ocean constructed from climate-model simulations of the 2090s but held constant in time  
46      for our analyses. Compared to typical predictions, these idealized states exhibit intense  
47      deep-ocean deoxygenation, for which we precisely quantify the contributions from changes  
48      in solubility, respiration, and ocean circulation. We find that deep-ocean deoxygenation

49 is driven by the slower circulation allowing respiration to act for 2–3 times longer thereby  
 50 overcoming lower respiration rates. The surface origin of oxygen shifts away from cold  
 51 high-latitude waters toward warmer waters, in which atmospheric oxygen is less solu-  
 52 ble, further reducing oxygen levels. Warming-driven decreases in solubility alone only  
 53 account for a mere 10 % of the total oxygen loss. The upper ocean remains well oxygenated  
 54 because changes in respiration and circulation compensate almost perfectly. Our results  
 55 highlight the central importance of circulation in controlling oxygen in the ocean.

## 56 1 Introduction

57 The ocean has lost an estimated ∼1–3 % of its oxygen content over the last 50 years  
 58 (e.g., Keeling & Garcia, 2002; Whitney et al., 2007; Helm et al., 2011; Schmidtko et al.,  
 59 2017; Breitburg et al., 2018; Bindoff et al., 2022; Roach & Bindoff, 2023; Ito et al., 2017;  
 60 Ito, 2022; Ito et al., 2024). Open-ocean deoxygenation is expected to continue in the fu-  
 61 ture because of global warming, which reduces oxygen solubility and deep-ocean venti-  
 62 lation (e.g., Matear et al., 2000; Keeling et al., 2010; Matear & Hirst, 2003; Bopp et al.,  
 63 2013; Long et al., 2019; Oschlies, 2021). There is broad consensus among models of the  
 64 sixth Coupled Model Intercomparison Project (CMIP6) that hypoxic zones will expand  
 65 over the next century (e.g., in the Pacific; Busecke et al., 2022) to varying degrees de-  
 66 pending on the future emissions' scenario (e.g., Kwiatkowski et al., 2020).

67 Ocean deoxygenation is increasingly recognized as posing an imminent threat to  
 68 global marine ecosystems and food security (e.g., Earle et al., 2018; Laffoley & Baxter,  
 69 2019). Oxygen is essential for life (e.g., Falkowski & Godfrey, 2008). Long-term expo-  
 70 sure to sufficiently low oxygen (severe hypoxia) can be lethal to marine organisms (e.g.,  
 71 Vaquer-Sunyer & Duarte, 2008; Diaz & Rosenberg, 2008). Mild to intermediate hypoxia  
 72 has important physiological, behavioral, and ecological effects on marine ecosystems (e.g.,  
 73 Ekau et al., 2010; Beman & Carolan, 2013; McCormick & Levin, 2017; Pascal et al., 2023;  
 74 Morée et al., 2023). Hence, the distribution of oxygen in the ocean is a key control on  
 75 shaping marine habitats (e.g., Rogers, 2000; Seibel, 2011; Stramma et al., 2012; Deutsch  
 76 et al., 2015; Sato et al., 2017; Franco et al., 2022; Mongwe et al., under review; Deutsch  
 77 et al., 2024). Even small O<sub>2</sub> declines and limited expansion of oxygen minimum zones  
 78 (OMZs) are a major concern for global-ocean health (e.g., Gallo & Levin, 2016; Wish-  
 79 ner et al., 2018; Deutsch et al., 2024).

80 Deoxygenation is driven by complex interactions among physical and biogeochemical  
81 processes that interact non-linearly on global scales. Oxygen in the ocean is controlled  
82 by air-sea exchange through surface winds and O<sub>2</sub> solubility, by photosynthetic produc-  
83 tion in the surface ocean, by bacterial respiration, and by the circulation which venti-  
84 lates the ocean and connects these processes through the transport of dissolved oxygen  
85 to the deep ocean (e.g., Oschlies et al., 2018; Levin, 2018). To attribute O<sub>2</sub> changes quan-  
86 titatively to specific driving mechanisms, a typical approach is to partition dissolved O<sub>2</sub>  
87 concentrations into a saturation concentration and apparent oxygen utilization (AOU;  
88 e.g., Bopp et al., 2002; Schmidtko et al., 2017; Couespel et al., 2019; Long et al., 2019;  
89 Busecke et al., 2022; Takano et al., 2023). To correct for AOU biases propagated by in-  
90 complete surface O<sub>2</sub> saturation (Ito et al., 2004), another common approach (using mod-  
91 els) is to compute preformed oxygen and “true” oxygen utilization (TOU; e.g., Oschlies  
92 et al., 2019; Palter & Trossman, 2018; Buchanan & Tagliabue, 2021; Cliff et al., 2021;  
93 Ito et al., 2022). Studies based on these approaches agree qualitatively that increased  
94 oxygen utilization drives most of the deoxygenation, with reduced solubility accounting  
95 for less than 50 % of upper-ocean deoxygenation, and less than ~25 % of the deoxygenation  
96 of the entire water column. However, how much of the AOU (or TOU) increase can  
97 be attributed to changes in ventilation (i.e., circulation) versus respiration remains un-  
98 clear (e.g., Breitburg et al., 2018; Oschlies et al., 2018).

99 While the importance of circulation for open-ocean hypoxia was recognized long  
100 ago (e.g., Wyrtki, 1962; Sarmiento et al., 1988), its precise contribution to changes in pre-  
101 formed O<sub>2</sub> and oxygen utilization has yet to be quantified (Oschlies et al., 2018). This  
102 is a challenging task because disentangling the effects of circulation changes from the ef-  
103 fects of changes in solubility and upstream respiration requires a careful accounting of  
104 all possible oxygen pathways and losses. To avoid these difficulties, some studies resort  
105 to perturbation experiments, under the tacit assumption that the system is sufficiently  
106 linear to infer the thermal and physical contributions to deoxygenation from the differ-  
107 ence between perturbed and unperturbed simulations. These perturbed simulations may  
108 consist, for example, in keeping surface solubility fixed in time (e.g., Matear et al., 2000;  
109 Matear & Hirst, 2003; Couespel et al., 2019), in keeping oxygen utilization rates (OUR)  
110 fixed in time (e.g., Deutsch et al., 2006), in removing biogeochemical processes (e.g., Cliff  
111 et al., 2021), or in a combination of the above (e.g., Plattner et al., 2001; Bopp et al.,  
112 2002). To assess circulation control on oxygen loss, other perturbations consist in keep-

113       ing the circulation fixed in its preindustrial state (e.g., Palter & Trossman, 2018). Such  
 114       residual-based perturbation approaches can be strongly biased by spatial correlations be-  
 115       tween changes in solubility and changes in circulation that are typically ignored. How-  
 116       ever, as we show here, such correlations can be of first order for large perturbations or  
 117       over long timescales. Also commonly used for assessing the effects of circulation changes  
 118       on deoxygenation is the ideal mean age, often invoked as an empirical timescale linking  
 119       TOU and OUR (e.g., Bopp et al., 2017; Palter & Trossman, 2018; Busecke et al., 2022).  
 120       However, all the studies mentioned above ultimately fall short of accurately attributing  
 121       deoxygenation to its drivers because they lack a quantitative framework, based on the  
 122       underlying fundamental equations, that connects TOU to OUR with the correct circu-  
 123       lation timescale.

124       Here, we address the following question: What would happen to oxygen if ocean  
 125       biogeochemistry were allowed to equilibrate with a 2090s circulation that was frozen in  
 126       time? To this end, we consider idealized steady oxygen cycles obtained by embedding  
 127       the intermediate-complexity PCO<sub>2</sub> biogeochemistry model (Pasquier et al., 2023) into  
 128       warmer and slower ocean states. These states are taken from climate-model simulations  
 129       for the 2090s and then held fixed (or “frozen”) in time for perpetuity. The equilibrated  
 130       steady-state oxygen cycle is obtained using a Newton solver and compared to preindus-  
 131       trial conditions. Equilibrated steady states allow us to probe the oxygen cycle on all the  
 132       fundamental timescales of the associated ocean transport (e.g., fast thermocline versus  
 133       slow abyssal ventilation). In particular, our approach captures the very longest timescales  
 134       that cannot be probed with typical centennial-scale transient simulations. In addition,  
 135       steady states afford many computational advantages that we exploit extensively. Note,  
 136       however, that this framework does not capture natural variability on any timescale (e.g.,  
 137       seasonal, interannual).

138       We rigorously partition O<sub>2</sub> changes into contributions from circulation changes, sol-  
 139       ubility changes, and their spatial correlations by employing the exact timescale that con-  
 140       nects TOU to upstream OUR. Specifically, in steady state, the local OUR contribution  
 141       at location  $\mathbf{r}$  to the TOU content of an interior volume  $\Omega$  has recently been shown to  
 142       be  $\text{OUR}(\mathbf{r}) \times \Gamma_{\Omega}^{\uparrow}(\mathbf{r})$ , where  $\Gamma_{\Omega}^{\uparrow}(\mathbf{r})$  is the “upstream exposure time”, i.e., the time that  
 143       the water in  $\Omega$  spent sweeping past upstream location  $\mathbf{r}$ , and hence the time over which  
 144       OUR( $\mathbf{r}$ ) acts (Holzer, 2022). Importantly,  $\Gamma_{\Omega}^{\uparrow}$  is a fundamental timescale of the circu-

145 lation only. Furthermore, we show here that  $\Gamma_\Omega^\uparrow$  also connects the preformed O<sub>2</sub> content  
 146 of  $\Omega$  to its surface origin.

147 Our idealized biogeochemical steady states exhibit intense abyssal deoxygenation  
 148 because of perpetually reduced ventilation and throttled Antarctic Bottom Water (AABW)  
 149 formation (Holzer et al., 2020), which stands in stark contrast to typical transient sim-  
 150 ulations of the late 21st century. While our idealized states cannot capture realistic tran-  
 151 sient evolution, they nevertheless inform us on the long-timescale mechanisms that drive  
 152 deoxygenation. We find that the intense abyssal deoxygenation in our idealized steady  
 153 states is characterized by widespread expansion of mild to severe hypoxia. Above 500 m  
 154 depth, hypoxic regions do not expand appreciably because decreases in preformed oxy-  
 155 gen are compensated by colocated TOU reductions, driven primarily by reduced respi-  
 156 ration rates. Below 2000 m depth, by contrast, strong increases in TOU are predominantly  
 157 driven by the slower perpetual 2090s circulation allowing respiration to act 2 to 3 times  
 158 longer. Preformed oxygen declines almost everywhere, driven primarily by equatorward  
 159 shifts in ventilation caused by reduced AABW and North Atlantic Deep Water (NADW)  
 160 formation, with reduced solubility only playing a secondary role (order 10 % of the to-  
 161 tal oxygen loss). Our analyses highlight the overarching importance of the circulation  
 162 in determining the ocean's oxygen content through its control on ventilation patterns  
 163 and the path-integrated oxygen utilization.

## 164 2 Methods

### 165 2.1 Frozen-in-time preindustrial and 2090s ocean circulations

166 We consider three idealized ocean states that are frozen in time: a preindustrial  
 167 state that is used as the reference and two perpetually warmer and slower ocean states.  
 168 Specifically, we use decadal averages of simulations from the Australian Community Cli-  
 169 mate and Earth System Simulator (ACCESS1.3; Marsland et al., 2013; Bi et al., 2013).  
 170 Decadal mean circulation and thermodynamic state variables (including temperature and  
 171 salinity) are then held constant in time for perpetuity. The 1990s decadal average is used  
 172 as an approximation for the preindustrial state, and 2090s decadal averages correspond-  
 173 ing to an intermediate and a worst-case climate-change scenario (Representative Con-  
 174 centration Pathways RCP4.5 and RCP8.5; Meinshausen et al., 2011, 2020) are used to  
 175 represent the perpetually warmer and slower ocean states. For further details, see the

work of Pasquier et al. (2024), who used the same framework of steady-state biogeochemistry embedded in frozen-in-time circulations to quantify carbon-cycle changes.

We emphasize that we do not assume that our perpetual-2090s circulations corresponds to a steady state of the ocean dynamics. Instead, we simply freeze the mean 2090s ocean state in time and analyze the idealized steady-state oxygen cycle that is in equilibrium with this perpetually slower and warmer ocean. Our results thus cannot be interpreted as predictions of the future. However, despite our idealized framework requiring a number of caveats (Section 4.1), our results inform us on the key mechanisms that drive deoxygenation in the real ocean. Working with steady states has several advantages, the most important of which is that it allows us to capture the biogeochemical response on the longest timescales of the circulation. In addition, steadiness has the practical advantages of obviating the need for time stepping and avoiding the complications of transience. In particular, steadiness made it possible to precisely decompose and separate the drivers of deoxygenation.

The advective–diffusive flux-divergence operator of each state is organized into a sparse transport matrix following Chamberlain et al. (2019). The horizontal advective fluxes were directly averaged from the ACCESS1.3 output while the vertical advective fluxes were inferred from mass conservation by integrating the horizontal divergence upward from the seafloor. Horizontal and vertical diffusion is included in the transport matrix with background diffusivities of  $500 \text{ m}^2 \text{ s}^{-1}$  (horizontal) and  $10^{-5} \text{ m}^2 \text{ s}^{-1}$  (vertical), and a mixed-layer vertical diffusivity of  $0.1 \text{ m}^2 \text{ s}^{-1}$ . To construct the transport matrix, we used the decadal mean of the yearly maximum mixed-layer depth as simulated by ACCESS1.3. The model grid employed (coarse-grained from the original ACCESS1.3 grid) has a nominal horizontal resolution of  $2^\circ \times 2^\circ$  (finer in the tropics) and 50 vertical levels with thicknesses increasing from 10 m at the surface to 335 m at depth. We used the same horizontal and vertical diffusivities for the preindustrial and 2090s states, and all our calculations account for both advection and diffusion.

When interpreting our results it is important to note that like most state-of-the-art climate models, the ACCESS1.3 circulation features an unrealistically deep mixed layer in the Southern Ocean compared to observations (de Boyer Montégut et al., 2004; Bi et al., 2013; de Lavergne et al., 2014). For the ACCESS1.3 simulations we used, the mixed layers reach below 5000 m near the Weddell and Ross Seas in the 1990s and strongly

shoal in the 2090s, which imprints on our results. Although abyssal ventilation and bottom-water formation through convection are unrealistic (e.g., Heuzé et al., 2013), the key realistic model behavior for our purposes here is a decline in Southern Ocean deep ventilation driven by climate change: Antarctic Bottom Water formation has been observed to decline in recent decades and is predicted to decline strongly over the next few decades (e.g., de Lavergne et al., 2014; Chen et al., 2023; Gunn et al., 2023; Li et al., 2023). (Detailed caveats of the circulation model are discussed in Section 4.1.)

## 215        2.2 Oxygen model

216        We use the PCO<sub>2</sub> biogeochemistry model of Pasquier et al. (2023). PCO<sub>2</sub> is em-  
217        bedded in the frozen-in-time ocean circulations using our transport matrices, and we solve  
218        directly for the biogeochemical steady state using a Newton solver. Our steady-state oxy-  
219        gen cycles thus correspond to the equilibrium that would ultimately be reached if the  
220        2090s thermodynamic and physical state of the ocean were held fixed in time for per-  
221        petuity.

222        A key feature of PCO<sub>2</sub> for capturing the response of dissolved oxygen to a change  
223        in ocean state is that PCO<sub>2</sub> explicitly models the nonlinear interactions and feedbacks  
224        between oxygen, carbon, and nutrients. This includes the effects of oxygen and partic-  
225        ulate organic matter on respiration, and the effects of temperature on biological produc-  
226        tion and respiration. The biogeochemical parameters of PCO<sub>2</sub> were objectively optimized  
227        for preindustrial conditions against observations of phosphate, dissolved inorganic car-  
228        bon, total alkalinity, and oxygen. (The same parameter values were then used for all our  
229        states.) The optimized O<sub>2</sub> field has a global volume-weighted root-mean-square model–  
230        observations mismatch of  $\sim$ 30  $\mu\text{M}$  (Pasquier et al., 2023). Systematic biases, in part in-  
231        herited from the parent ACCESS-model circulation, remain despite parameter optimiza-  
232        tion, with underestimated O<sub>2</sub> in the upper tropical Pacific and Atlantic above  $\sim$ 1000 m  
233        and overestimated O<sub>2</sub> in the Southern Ocean and in the tropical Indian Ocean (see Ap-  
234        pendix Fig. A1 for a comparison between modelled and observed zonal mean  $p\text{O}_2$ ). We  
235        deem these biases acceptable as they are smaller than for most CMIP5 models (Bao &  
236        Li, 2016) and because they are generally dwarfed by the much larger changes analyzed  
237        here.

238 In the PCO<sub>2</sub> model, oxygen enters and exits the ocean through air-sea gas exchange,  
 239 is photosynthetically produced in the euphotic layer, and utilized through aerobic bac-  
 240 terial respiration. In steady state, the three-dimensional O<sub>2</sub> concentrations obeys

241  $\mathcal{T} \text{O}_2 = P - \text{OUR} + J_{\text{atm}}, \quad (1)$

242 where the frozen-in-time transport operator  $\mathcal{T}$  acts on O<sub>2</sub> concentrations such that  $\mathcal{T} \text{O}_2 =$   
 243  $\nabla \cdot (\mathbf{u} \text{O}_2) - \nabla \cdot \mathbf{K} \nabla \text{O}_2$  is the divergence of the advective-diffusive flux of O<sub>2</sub> due to ve-  
 244 locity  $\mathbf{u}$  and eddy diffusion (diffusivity tensor  $\mathbf{K}$ ).  $P = r_{\text{O}_2:\text{C}} U_{\text{C}}$  is the photosynthetic  
 245 production of oxygen keyed to biological carbon uptake  $U_{\text{C}}$  through the optimized  $r_{\text{O}_2:\text{C}} =$   
 246 1.31 molO<sub>2</sub> molC<sup>-1</sup>, and OUR =  $r_{\text{O}_2:\text{C}} (R_{\text{DOC}} + R_{\text{POC}}) \Theta(\text{O}_2 - \text{O}_2^{\text{lim}})$  is the oxygen uti-  
 247 lization rate keyed to respiration of dissolved and particulate organic carbon ( $R_{\text{DOC}}$  and  
 248  $R_{\text{POC}}$ ). (The  $\Theta$  term switches off aerobic respiration when O<sub>2</sub> drops below  $\text{O}_2^{\text{lim}} = 5 \mu\text{M}$ ,  
 249 implicitly representing the effect of anaerobic denitrification.) Air-sea gas exchange is  
 250 modelled using the parameterization  $J_{\text{atm}} = k (K_0 p\text{O}_2^{\text{atm}} - \text{O}_2)/h$  at the surface (Wan-  
 251 ninkhof, 2014), where  $k$  is the wind- and temperature-dependent gas-transfer velocity,  
 252  $K_0$  is the temperature- and salinity-dependent oxygen solubility,  $p\text{O}_2^{\text{atm}}$  is the oxygen  
 253 atmospheric partial pressure (based on an atmospheric oxygen mixing ratio of 0.210 for  
 254 both preindustrial and perpetual-2090s states), and  $h = 10 \text{ m}$  is the thickness of the top  
 255 model layer. (See Section 4.1 for discussion on the caveats of the biogeochemistry model.)

256 We organize the grid values of concentrations into column vectors and discretized  
 257 linear operators into corresponding sparse matrices. The nonlinear system of biogeochem-  
 258 ical tracer equations is solved for steady state using a Newton solver. In matrix form,  
 259 the vector of oxygen concentrations,  $\mathbf{O}_2$ , is the solution to  $\mathbf{T} \mathbf{O}_2 = \mathbf{P} - \mathbf{OUR} + \mathbf{J}_{\text{atm}}$ ,  
 260 where  $\mathbf{T}$  is the discretized advective-diffusive flux-divergence operator (“transport ma-  
 261 trix” for short) such that  $\mathbf{T} \mathbf{O}_2$  is the vector of the divergence of the advective-diffusive  
 262 flux of oxygen, and  $\mathbf{P}$ ,  $\mathbf{OUR}$ , and  $\mathbf{J}_{\text{atm}}$  are the vectors of photosynthetic oxygen pro-  
 263 duction, oxygen utilization, and air-sea oxygen exchange, respectively.

### 264 2.3 Preformed oxygen, O<sub>2</sub><sup>pre</sup>

265 Preformed oxygen is defined here as the oxygen that would be propagated by the  
 266 ocean circulation out of the euphotic-layer and into the ocean’s interior in the absence  
 267 of any aphotic sources and sinks. We use the base of the euphotic zone rather than the  
 268 base of the mixed layer to define preformed oxygen for convenience and consistency with

269 the definitions of preformed and regenerated phosphate and carbon in the related work  
 270 of Pasquier et al. (2023, 2024). Hence,  $O_2^{\text{pre}}$  depends only on euphotic  $O_2$  concentrations  
 271 and on ventilation patterns.

272 In matrix form, the vector of preformed oxygen concentrations,  $\mathbf{O}_2^{\text{pre}}$ , is conveniently  
 273 computed by solving  $(\mathbf{T} + \mathbf{L}) \mathbf{O}_2^{\text{pre}} = \mathbf{L} \mathbf{O}_2$ , where  $\mathbf{L}$  is a diagonal matrix with diag-  
 274 onal values of  $1 \text{ s}^{-1}$  in the euphotic zone and 0 otherwise, enforcing  $O_2^{\text{pre}} = O_2$  in the eu-  
 275 photic zone (only the euphotic-zone values of  $\mathbf{O}_2$  are used in  $\mathbf{L} \mathbf{O}_2$ ). (For such short re-  
 276 laxation time, there is no sensitivity to its precise value; 10 s gives indistinguishable re-  
 277 sults.)

278 To separate the effects of solubility from the effects of circulation on  $O_2$  within the  
 279 euphotic zone, we further decompose  $O_2^{\text{pre}}$  into a saturated component  $O_2^{\text{sat}}$  and a dis-  
 280 equilibrium component  $O_2^{\text{dis}} = O_2^{\text{pre}} - O_2^{\text{sat}}$ . This decomposition is useful because the  
 281 air-sea  $O_2$  disequilibrium varies with location and can be important in deep-water for-  
 282 mation regions (see, e.g., Russell & Dickson, 2003; Ito et al., 2004; Duteil et al., 2013;  
 283 Eggleston & Galbraith, 2018).

#### 284 2.4 True oxygen utilization, TOU

285 To quantify the oxygen deficit caused by respiration, we use “true oxygen utiliza-  
 286 tion”  $\text{TOU} = O_2^{\text{pre}} - O_2$  (e.g., Broecker & Peng, 1982; Ito et al., 2004; Koeve & Kähler,  
 287 2016; Holzer, 2022). TOU is thus the cumulated amount of oxygen that has been removed  
 288 by respiration along its interior transit since leaving the euphotic zone. The vector of  
 289 TOU grid values is computed similarly to  $O_2^{\text{pre}}$  by solving  $(\mathbf{T} + \mathbf{L}) \mathbf{TOU} = \mathbf{OUR}$  (Holzer,  
 290 2022). Note that  $-\text{TOU}$  may also be thought of as regenerated oxygen,  $O_2 - O_2^{\text{pre}}$  (e.g.,  
 291 DeVries & Deutsch, 2014).

#### 292 2.5 Deoxygenation drivers

293 To summarize the contributions to deoxygenation from changes in circulation, sol-  
 294 ubility, or respiration, it is useful to integrate the oxygen change over a specific volume  
 295  $\Omega$  of interest. We will first consider TOU and then  $O_2^{\text{pre}}$ .

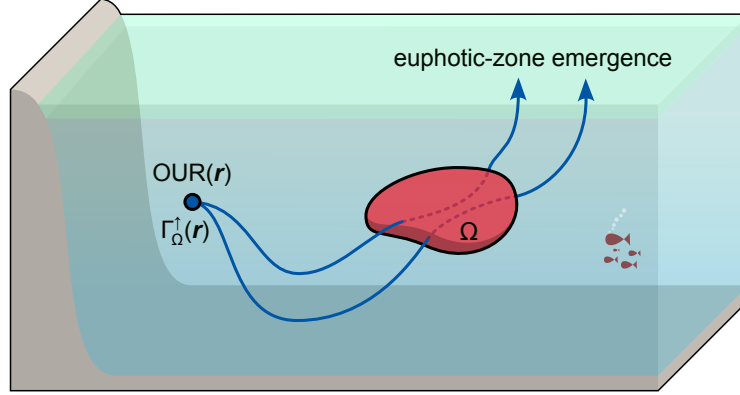


**Figure 1.** The upstream exposure time at any interior location  $\mathbf{r}$  (blue dot) is the time that water currently in interior volume  $\Omega$  (red region) spent at  $\mathbf{r}$  in the past (integrated over all paths and past times; blue lines). It is thus the total time for which the water in  $\Omega$  was exposed to oxygen utilization at upstream location  $\mathbf{r}$  in the past. This allows us to connect the oxygen “missing” in  $\Omega$  (the  $\Omega$ -integrated TOU) to the oxygen utilization rate (OUR) at  $\mathbf{r}$ . In steady state, this upstream exposure time equals  $\Gamma_{\Omega}^{\uparrow}(\mathbf{r})$ , the mean time that water currently at location  $\mathbf{r}$  will spend in  $\Omega$  on its way to the euphotic zone (see also Eq. (2) and Holzer, 2022).

296

### 2.5.1 Change in TOU

297

The  $\Omega$  inventory of TOU is controlled at every location  $\mathbf{r}$  upstream of  $\Omega$  by  $\text{OUR}(\mathbf{r})$  and by the time that the water currently in  $\Omega$  spent flowing past  $\mathbf{r}$ , which is the time for which  $\text{OUR}(\mathbf{r})$  acts on the oxygen heading toward  $\Omega$ . This timescale, which we call “upstream exposure time” here, was only recently derived and computed by Holzer (2022), who showed that for steady flow it is equal to  $\Gamma_{\Omega}^{\uparrow}(\mathbf{r})$ , the mean time that water currently at  $\mathbf{r}$  will spend in  $\Omega$  on its way to the surface (Fig. 1). In steady state,  $\Gamma_{\Omega}^{\uparrow}(\mathbf{r})$  equals the time that oxygen at  $\mathbf{r}$  was exposed to respiration upstream of  $\Omega$  and connects the TOU inventory to  $\text{OUR}(\mathbf{r})$  through the relationship (Holzer, 2022):

305

$$\int_{\Omega} \text{TOU}(\mathbf{r}) d^3\mathbf{r} = \int \text{OUR}(\mathbf{r}) \Gamma_{\Omega}^{\uparrow}(\mathbf{r}) d^3\mathbf{r}. \quad (2)$$

306

We emphasize that the upstream exposure time ( $\Gamma_{\Omega}^{\uparrow}$  in steady state) is fundamentally different from the ideal mean age (e.g., Primeau, 2005), which is commonly used to approximately relate TOU or AOU to OUR (e.g., Doney & Bullister, 1992; Warner et al., 1996; Zheng et al., 1997; Feely et al., 2004; Bopp et al., 2017; Palter & Trossman, 2018, to cite a few), despite known systematic biases (e.g., Duteil et al., 2013; Sonnerup et al.,

311 2013; Brandt et al., 2015; Sonnerup et al., 2015; Koeve & Kähler, 2016; Thomas et al.,  
 312 2020).

313 The integrals in Eq. (2) are easily computed in matrix form. That is, Eq. (2) can  
 314 be written as  $\boldsymbol{\Omega}^T \mathbf{V} \mathbf{T} \mathbf{O} \mathbf{U} = \mathbf{O} \mathbf{U} \mathbf{R}^T \mathbf{V} \mathbf{I}_\Omega^\uparrow$ , where  $\mathbf{V}$  is a diagonal matrix with the grid-  
 315 box volumes along the diagonal,  $\boldsymbol{\Omega}$  is a mask vector with entries of 1 for grid cells in  $\Omega$   
 316 and entries of 0 otherwise, and the  $T$  superscript denotes the matrix transpose. The up-  
 317 stream exposure time obeys  $(\tilde{\mathbf{T}} + \mathbf{L}) \mathbf{I}_\Omega^\uparrow = \boldsymbol{\Omega}$  (Holzer, 2022), where  $\tilde{\mathbf{T}} = \mathbf{V}^{-1} \mathbf{T}^T \mathbf{V}$  is  
 318 the volume-weighted adjoint of  $\mathbf{T}$ , which governs the time-reversed adjoint flow.

319 The connection of TOU with OUR through  $\mathbf{I}_\Omega^\uparrow$  in Eq. (2) allows us to partition TOU  
 320 changes into contributions from changes in respiration, circulation, and their interaction.  
 321 Specifically, we algebraically decompose, at every point  $\mathbf{r}$  of the ocean, the change in the  
 322 integrand ( $\mathbf{O} \mathbf{U} \mathbf{R} \times \mathbf{I}_\Omega^\uparrow$ ) on the right-hand-side of Eq. (2) as

$$323 \Delta(\mathbf{O} \mathbf{U} \mathbf{R} \times \mathbf{I}_\Omega^\uparrow) = \underbrace{\mathbf{I}_\Omega^\uparrow \Delta \mathbf{O} \mathbf{U} \mathbf{R}}_{\text{respiration}} + \underbrace{\mathbf{O} \mathbf{U} \mathbf{R} \Delta \mathbf{I}_\Omega^\uparrow}_{\text{circulation}} + \underbrace{\Delta \mathbf{O} \mathbf{U} \mathbf{R} \Delta \mathbf{I}_\Omega^\uparrow}_{\text{cross term}}, \quad (3)$$

324 where a quantity  $X$  not preceded by  $\Delta$  denotes its preindustrial value and  $\Delta X$  denotes  
 325 the change in  $X$  for the state embedded in the perpetual-2090s circulations. The driv-  
 326 ing process represented by each term is indicated beneath the braces of Eq. (3), and these  
 327 terms are globally integrated to give the corresponding contributions to the changes in  
 328 the  $\Omega$  inventory of TOU in accord with Eq. (2). The  $\mathbf{I}_\Omega^\uparrow \Delta \mathbf{O} \mathbf{U} \mathbf{R}$  term corresponds to the  
 329 contribution from respiration-only changes, with the circulation fixed at its preindustrial  
 330 state, while  $\mathbf{O} \mathbf{U} \mathbf{R} \Delta \mathbf{I}_\Omega^\uparrow$  corresponds to the contribution from circulation-only changes,  
 331 with  $\mathbf{O} \mathbf{U} \mathbf{R}$  fixed at its preindustrial value, and the “cross term”  $\Delta \mathbf{O} \mathbf{U} \mathbf{R} \Delta \mathbf{I}_\Omega^\uparrow$  corresponds  
 332 to the colocated changes in  $\mathbf{O} \mathbf{U} \mathbf{R}$  and  $\mathbf{I}_\Omega^\uparrow$ . To the best of our knowledge, this is the first  
 333 decomposition to cleanly separate respiration-only and circulation-only effects, and to  
 334 explicitly account for the effect of concurrent changes in both respiration and circula-  
 335 tion.

### 336 2.5.2 Change in $O_2^{\text{pre}}$

337 In steady state, the  $\Omega$  inventory of preformed oxygen is determined by euphotic oxy-  
 338 gen concentrations modulated by the amount of  $\Omega$ -volume ventilated per unit area at  
 339 the base of the euphotic zone,  $\mathcal{V}_\Omega^\downarrow$ . Mathematically,

$$340 \int_\Omega O_2^{\text{pre}}(\mathbf{r}) d^3 \mathbf{r} = \int O_2(\mathbf{r}_s) \mathcal{V}_\Omega^\downarrow(\mathbf{r}_s) d^2 \mathbf{r}_s, \quad (4)$$

341 where location  $\mathbf{r}_s$  ranges over the base of the euphotic layer. The matrix form of Eq. (4)  
 342 is  $\boldsymbol{\Omega}^\top \mathbf{V} \mathbf{O}_2^{\text{pre}} = \mathbf{O}_2^\top \mathbf{A} \mathcal{V}_\Omega^\downarrow$  where  $\mathbf{A}$  is a diagonal matrix with the horizontal area of each  
 343 grid cell along the diagonal and where  $\mathcal{V}_\Omega^\downarrow = \mathbf{A}^{-1} \mathbf{L} \mathbf{V} \boldsymbol{\Gamma}_\Omega^\uparrow$ . One can derive these re-  
 344 lationships by noting that just like  $\mathbf{OUR}$  is the source term for  $\mathbf{TOU}$ , the equation for  
 345 preformed oxygen shows that  $\mathbf{L} \mathbf{O}_2$  is the effective source term for  $\mathbf{O}_2^{\text{pre}}$ . By replacing  
 346  $\mathbf{OUR}$  with  $\mathbf{L} \mathbf{O}_2$  and  $\mathbf{TOU}$  with  $\mathbf{O}_2^{\text{pre}}$  in the matrix form of Eq. (2), we obtain  $\boldsymbol{\Omega}^\top \mathbf{V} \mathbf{O}_2^{\text{pre}} =$   
 347  $\mathbf{O}_2^\top \mathbf{L} \mathbf{V} \boldsymbol{\Gamma}_\Omega^\uparrow$ . This relationship provides a direct connection between the  $\mathbf{O}_2^{\text{pre}}$  inventory  
 348 of  $\Omega$  and the flux of  $\boldsymbol{\Gamma}_\Omega^\uparrow$  into the euphotic zone, because  $\boldsymbol{\Gamma}_\Omega^\uparrow$  traces the  $\mathbf{O}_2^{\text{pre}}$  in  $\Omega$  back to  
 349 its euphotic origin. (We note in passing that this link stems from the equivalence between  
 350 concentration propagated forward in time from a boundary condition and the flux into  
 351 that boundary from a unit-injected mass propagated in the time-reversed adjoint flow  
 352 (e.g., Holzer & Hall, 2000).)

353 The  $\Omega$  volume ventilated per unit area  $\mathcal{V}_\Omega^\downarrow$  is a generalization of the ocean volume  
 354 ventilated per unit area (e.g., Primeau, 2005; Holzer et al., 2020).  $\mathcal{V}_\Omega^\downarrow$  provides a quan-  
 355 titative connection between the  $\Omega$  inventory of  $\mathbf{O}_2^{\text{pre}}$  and euphotic  $\mathbf{O}_2$  concentrations. We  
 356 note in passing that  $\mathcal{V}_\Omega^\downarrow$  is proportional to the volume fractions  $f_{ij}$  derived by Fu et al.  
 357 (2018) for quantifying OMZ ventilation, through  $f_{ij} = A_{ij} \mathcal{V}_\Omega^\downarrow / v_\Omega$ , where  $A_{ij}$  is the sur-  
 358 face grid cell area and  $v_\Omega$  is the  $\Omega$  volume.

359 Similar to our analysis of TOU changes, we partition changes in the  $\Omega$  inventory  
 360 of  $\mathbf{O}_2^{\text{pre}}$  into contributions from changes in solubility and circulation. To this end, we al-  
 361 gebraically decompose, at every point  $\mathbf{r}_s$  at the base of the euphotic layer, the change  
 362 in the integrand  $\mathbf{O}_2 \mathcal{V}_\Omega^\downarrow$  on the right-hand-side of Eq. (4) as

$$\Delta(\mathbf{O}_2 \mathcal{V}_\Omega^\downarrow) = \underbrace{\mathcal{V}_\Omega^\downarrow \Delta \mathbf{O}_2^{\text{sat}}}_{\text{solubility}} + \underbrace{\mathbf{O}_2^{\text{sat}} \Delta \mathcal{V}_\Omega^\downarrow}_{\text{circulation}} + \underbrace{\Delta(\mathbf{O}_2^{\text{dis}} \mathcal{V}_\Omega^\downarrow)}_{\text{cross term}}, \quad (5)$$

363 where we have further separated euphotic  $\mathbf{O}_2$  into its saturated and disequilibrium com-  
 364 ponents, and the corresponding driving processes are indicated with braces. The term  
 365  $\mathcal{V}_\Omega^\downarrow \Delta \mathbf{O}_2^{\text{sat}}$  accounts for the contribution to  $\Delta \mathbf{O}_2^{\text{pre}}$  in  $\Omega$  from solubility-only changes, keep-  
 366 ing the circulation (and thus ventilation volumes  $\mathcal{V}_\Omega^\downarrow$ ) fixed in its preindustrial state. The  
 367 contribution from circulation-only changes includes  $\mathbf{O}_2^{\text{sat}} \Delta \mathcal{V}_\Omega^\downarrow$ , where solubility in the eu-  
 368 photic zone is fixed at its preindustrial values, and  $\Delta(\mathbf{O}_2^{\text{dis}} \mathcal{V}_\Omega^\downarrow)$ , which we consider to be  
 369 a circulation-only effect by assuming that  $\mathbf{O}_2^{\text{dis}}$  is entirely driven by circulation changes.  
 370 The decomposition of Eq. (5) is, to the best of our knowledge, also new.

372        **2.6 Hypoxia severity categories**

373        To quantify the extent of low-oxygen conditions, we follow Hofmann et al. (2011)  
 374        and define hypoxia categories A, B, and C, ranging from mild to severe in terms of the  
 375        in situ effective partial pressure of oxygen,  $pO_2$ . Specifically for our model, category-A  
 376        mild hypoxia is deemed to occur where  $pO_2 \leq 100$  matm, category-B intermediate hy-  
 377        poxia where  $pO_2 \leq 50$  matm, and category-C severe hypoxia where  $pO_2 \leq 15$  matm.  
 378        Note that we have adjusted the  $pO_2 = 106, 60$ , and  $22$  matm thresholds of Hofmann  
 379        et al. (2011) such that the modelled global hypoxia volume for each category matches  
 380        the values based on GLODAPv2 observations (Lauvset et al., 2016). Despite matching  
 381        the global hypoxic volumes, the horizontal extent of hypoxic regions remain overestimated  
 382        in the Pacific and Atlantic and underestimated in the Indian Ocean (see Appendix Figs. A2  
 383        and A3 for more details).

384        **3 Results**

385        **3.1 Global deoxygenation and expansion of hypoxic regions**

386        We find intense deoxygenation for our steady-state oxygen cycles embedded in the  
 387        perpetual-2090s ocean states, with the global oxygen inventory decreasing by 30 % and  
 388        60 % for the RCP4.5- and RCP8.5-based states, respectively. Figure 2 shows the basin  
 389        zonal-mean  $pO_2$  for each scenario and the corresponding change from preindustrial to  
 390        perpetual-2090s states. (We show the effective partial pressure,  $pO_2$ , because it is the  
 391        most relevant thermodynamic oxygen quantity for critical physiological processes in liv-  
 392        ing organisms (Hofmann et al., 2011).) The oxygen loss is largest in the Pacific because  
 393        of the dramatically reduced ventilation from AABW. Oxygen loss is also intense in the  
 394        Atlantic sector of the Southern Ocean, but deoxygenation in the Atlantic is overall less  
 395        pronounced as the mid-depth North Atlantic remains ventilated by North Atlantic Deep  
 396        Water (NADW) in the perpetual-2090s circulations. Deoxygenation does not occur ev-  
 397        erywhere however, with slight increases in the zonal mean  $pO_2$  occurring close to the sur-  
 398        face in each basin, particularly at northern mid-latitudes in the Atlantic and Indian Ocean  
 399        (Fig. 2j–o), likely due to reduced local respiration and shoaling NADW.

400        The expansion of hypoxic zones depends strongly on the severity (i.e.,  $pO_2$  thresh-  
 401        old) of hypoxia considered, on the local ventilation, and on the climate-change scenario.  
 402        Figure 3 shows the profiles of the spatial extent of each hypoxia category (Methods, Sec-

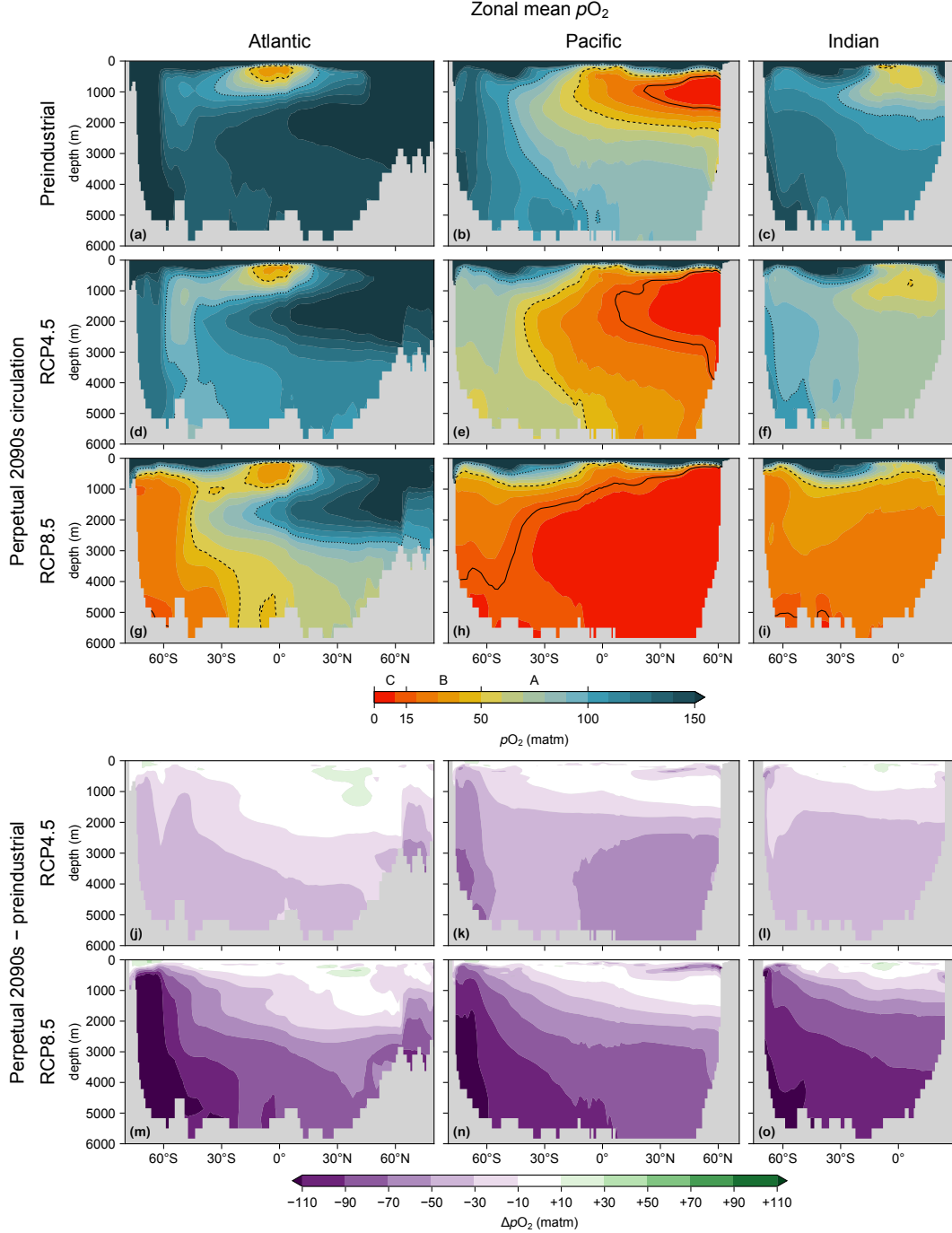


**Figure 2.** (a) Atlantic, (b) Pacific, and (c) Indian Ocean zonal-mean  $p\text{O}_2$  for the preindustrial state. The dotted, dashed, and solid contour lines indicate the  $p\text{O}_2 = 100$ , 50, and 15 matm thresholds of hypoxia categories A, B, and C, respectively. (d–f) As (a–c) for the state with perpetual-2090s circulation of the RCP4.5 scenario. (g–i) As (d–f) for RCP8.5. (j–o) As (d–i) for the change from the preindustrial state to the perpetual-2090s states. The Atlantic basin excludes the Gulf of Mexico and the Caribbean, and the Pacific basin excludes the Sea of Japan so that the zonal means are more cleanly interpretable.

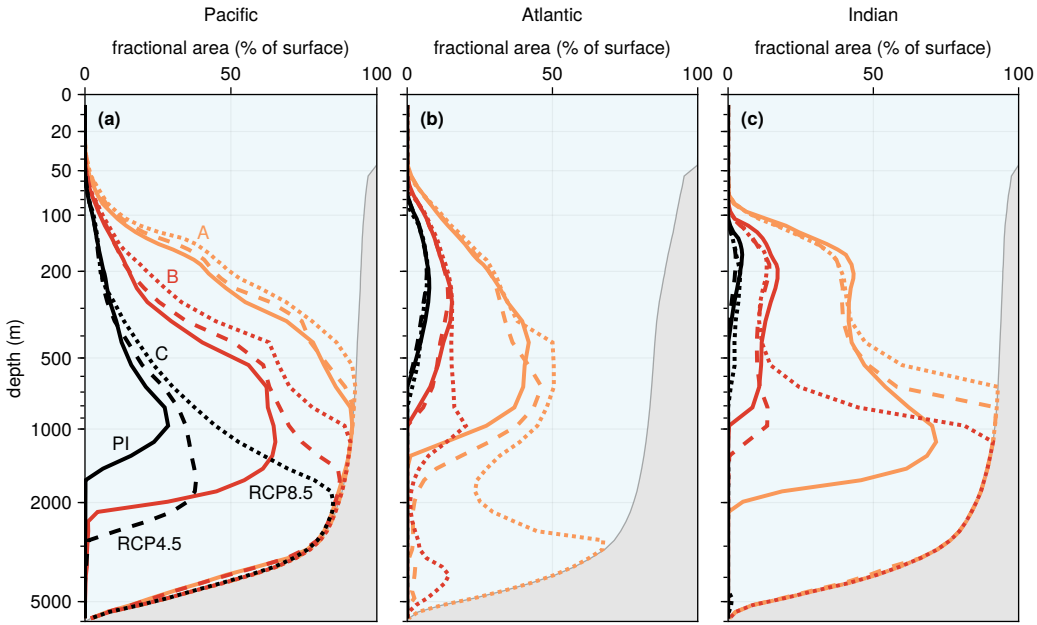


**Figure 3.** (a) Pacific depth profiles of the spatial extent of mild (A, orange;  $pO_2 \leq 100$  matm), intermediate (B, red;  $pO_2 \leq 50$  matm), and severe hypoxia (C, black;  $pO_2 \leq 15$  matm) for the preindustrial state (PI; solid lines), the perpetual RCP4.5 2090s state (dashed lines), and the perpetual RCP8.5 2090s state (dotted lines). The spatial extent for a given hypoxia category and depth is quantified by the ratio of the horizontal hypoxic area to the surface area of the corresponding ocean basin. (The gray area represents the seafloor.) (b) As (a) for the Atlantic. (c) As (a) for the Indian Ocean. Note the nonlinear depth scale.

403 tion 2.6), over each basin, and for each scenario. The expansion of hypoxic regions is larger  
 404 for RCP8.5 than for the less extreme RCP4.5 scenario. We find that low-oxygen condi-  
 405 tions generally expand toward the seafloor in the deep ocean rather than toward the sur-  
 406 face. In the Pacific, expansion is maximal with all abyssal waters becoming moderately  
 407 hypoxic (cat. B;  $pO_2 \leq 50$  matm) for RCP4.5 and severely hypoxic (cat. C;  $pO_2 \leq 15$  matm)  
 408 for RCP8.5. Similarly, all Indian Ocean waters below roughly 800 m become mildly hy-  
 409 poxic for RCP4.5 and moderately hypoxic for RCP8.5. In the Atlantic, the volume of  
 410 severe hypoxia changes little, while mild and intermediate hypoxia only strongly expand  
 411 for RCP8.5 at intermediate and abyssal depths. In the Atlantic and Indian Ocean above  
 412 500 m, the areal extent of hypoxia actually contracts slightly as  $pO_2$  has slight increases  
 413 there (cf., Fig. 2j-o discussed above).

To visualize the horizontal distribution of expanding hypoxic conditions, we consider the vertical water-column minimum  $pO_2$  shown in Fig. 4. In the preindustrial state, oxygen minimum zones are located in the eastern tropical sectors of the major basins and in the North Pacific. In the perpetual-2090s states, global-scale expansion of low-oxygen conditions is visible for RCP4.5, except in the North Atlantic and in the Atlantic sector of the Southern Ocean, which remain ventilated ( $pO_2 \geq 100$  matm) by NADW and AABW. Intermediate hypoxia expands southward beyond southern mid-latitudes, while severe hypoxia expands into the tropics. For the RCP8.5-based state, mild hypoxia occurs across the entire global ocean (although predominantly at depth as shown in Fig. 3), while intermediate hypoxia occurs across the entire Pacific, South Atlantic, and Indian Ocean, and severe hypoxia extends across the entire Pacific only, reaching as far as the Southern Ocean.

### 3.2 Drivers of deoxygenation

#### 3.2.1 Changes in TOU and preformed oxygen

Deoxygenation occurs through declines in preformed oxygen and through increases in true oxygen utilization (TOU; see Methods, Section 2), which may also be thought of as negative regenerated oxygen (i.e.,  $O_2^{\text{reg}} = -\text{TOU}$ ; see, e.g., DeVries & Deutsch, 2014). Qualitatively, reduced respiration drives TOU decreases while a slower circulation drives TOU increases by allowing more time for respiration to act. Thus, TOU can either increase or decrease (Appendix Fig. B1) depending on which effect dominates. We find that in the upper ocean TOU decreases because of reduced OUR and in the deep ocean TOU increases because of longer circulation timescales (upstream exposure times; Appendix Fig. B2). Preformed oxygen, by contrast, declines over most of the ocean (Appendix Fig. B1), in part because of warming-driven solubility decreases and importantly, as we will show below, because of an equatorward shift in ventilation. With warmer future sea surface temperature (SST), surface  $O_2$  concentrations decrease almost everywhere, except in the North Atlantic “cold blob” (e.g., Cheng et al., 2022) where temperatures decrease, and near the Weddell and Ross Seas where the mixed layer shoals (Appendix Fig. B3). Shoaling of the ACCESS model’s preindustrially deep mixed layer in these regions (see Fig. C2 in Pasquier et al., 2023) considerably increases surface residence times, allowing preindustrially undersaturated  $O_2$  to become more saturated despite the decreased solubility. (See Section 4.1 for caveats on the circulation model.)

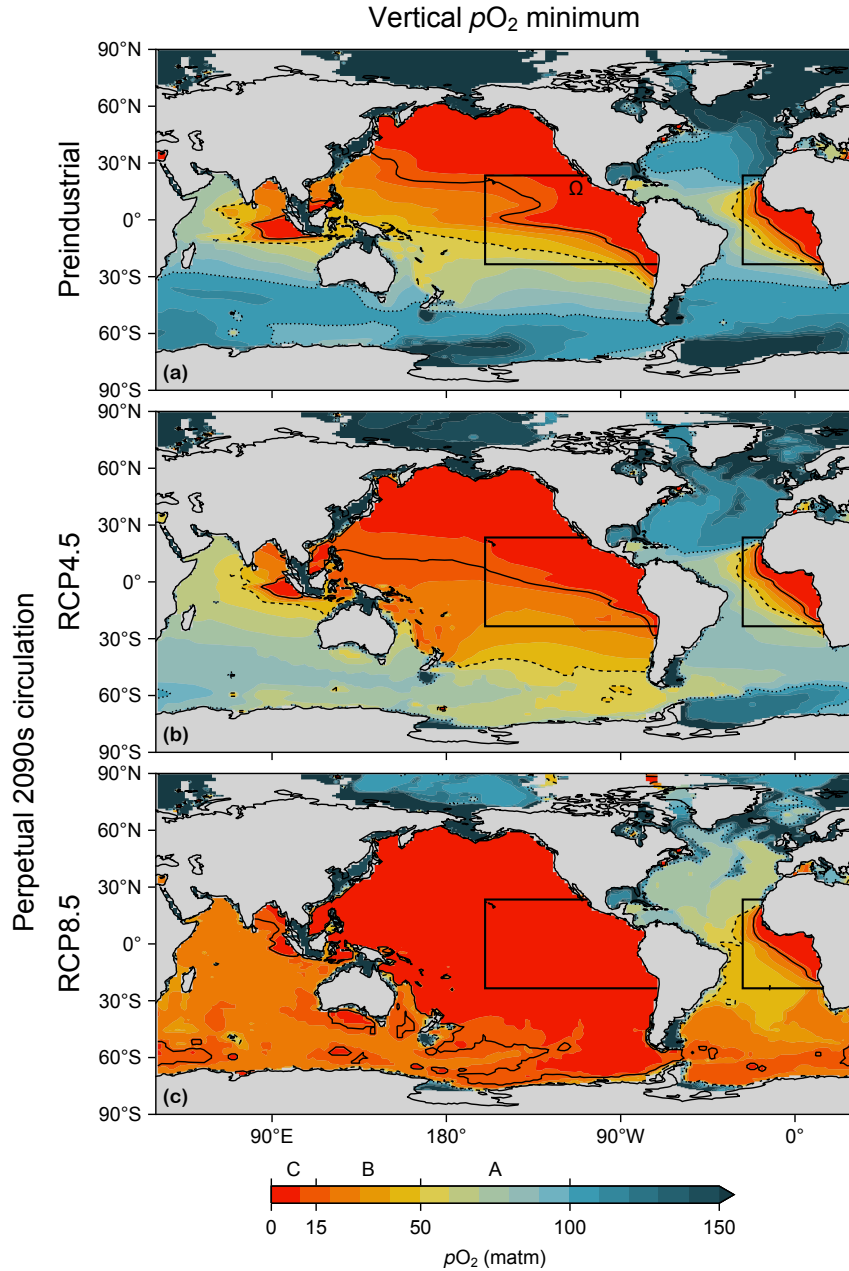


**Figure 4.** (a–c) Maps of the water-column minimum  $p\text{O}_2$  for (a) the preindustrial state, (b) the perpetual-2090s RCP4.5 state, and (c) the perpetual-2090s RCP8.5 state. The dotted, dashed, and solid contour lines indicate the  $p\text{O}_2 = 100$ , 50, and 15 matm thresholds of hypoxia categories A, B, and C, respectively. Also indicated are the eastern tropical Pacific and Atlantic  $\Omega$  regions over which our diagnostics are applied.

To analyze the drivers of deoxygenation in detail, we focus for definiteness on the eastern tropical Pacific (ETP, 23°S–23°N, east of 160°W) and eastern tropical Atlantic (ETA, 23°S–23°N, east of 27°W), as indicated in Fig. 4. Figure 5 shows the average  $O_2$  depth profiles in these regions and their decomposition into  $O_2^{\text{pre}}$  and TOU. In the preindustrial state, both the ETP and ETA are severely hypoxic in the depth range of 150–800 m and 150–400 m, respectively. In the perpetual-2090s steady states, we find small upper-ocean  $O_2$  decreases of about 10  $\mu\text{M}$  above 70 m, caused by a decrease in  $O_2^{\text{pre}}$ . Decreases in  $O_2^{\text{pre}}$  are approximately constant with depth below  $\sim$ 100 m, while  $\Delta\text{TOU}$  changes sign at  $\sim$ 1500 m in the ETP and at  $\sim$ 800 m in the ETA. Above  $\sim$ 500 m, the TOU decreases compensate almost perfectly for the  $O_2^{\text{pre}}$  decreases. Conversely, below  $\sim$ 2000 m, TOU increases and  $O_2^{\text{pre}}$  decreases compound, resulting in strong deoxygenation, with deep ETP  $O_2$  reduced to  $\sim$ 25 % of its preindustrial levels for RCP4.5 and to a mere  $\sim$ 5 % for RCP8.5. Deep ETA  $O_2$  decreases are of similar magnitude, but  $O_2$  levels are roughly 100  $\mu\text{M}$  higher in all states owing to North Atlantic ventilation.

We now partition the changes  $\Delta\text{TOU}$  and  $\Delta O_2^{\text{pre}}$  into contributions from the key drivers, that is, into contributions from changes in circulation, respiration, and solubility (Methods, Section 2.5). For this purpose, we narrow our focus to the ETP only — similar mechanisms are at play in the ETA, but will not be discussed here for brevity. Guided by the shape of their profiles in Fig. 5, we furthermore integrate over the upper ETP (above 500 m) and separately over the deep ETP (below 2000 m) to summarize how different drivers dominate at different depths. (For simplicity, we use the surface rather than the mixed- or euphotic-layer base as the top boundary of the upper ETP so that it occupies the same volume for all states.) The resulting attribution of  $\Delta\text{TOU}$  and  $\Delta O_2^{\text{pre}}$  to their drivers is shown in Fig. 6; we first discuss  $\Delta\text{TOU}$  and then  $\Delta O_2^{\text{pre}}$ .

### 3.2.2 Upper and deep ETP budgets of $\Delta\text{TOU}$

The average TOU over a given region  $\Omega$  is given by the global volume integral of the product of OUR with the upstream exposure time,  $\Gamma_\Omega^\uparrow$  in steady state (see Methods, Section 2, Eq. (2), and Fig. 1). This allows us to decompose  $\Delta\text{TOU}$  into contributions from changes in respiration, from changes in circulation, and from their spatial correlations, which we refer to as the “cross term” in Eq. (3). These contributions are shown as the first three colored bars in each panel of Fig. 6.

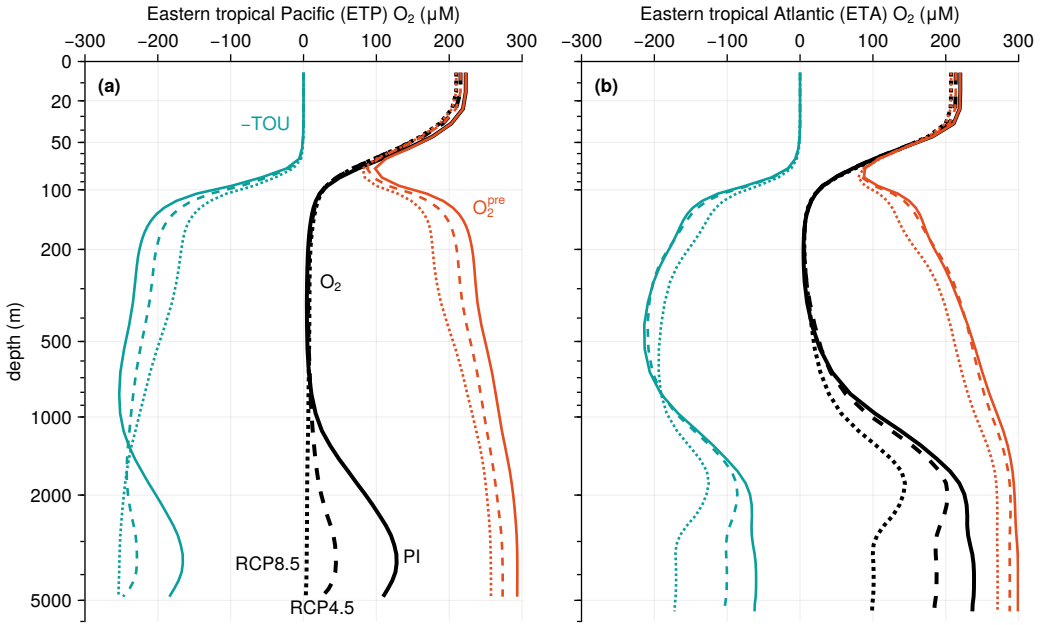


**Figure 5.** (a) Eastern tropical Pacific profiles of oxygen ( $O_2$ , black), preformed oxygen ( $O_2^{pre}$ , orange), and true oxygen utilization (TOU, teal) for the preindustrial state (PI; solid line), the perpetual-2090s RCP4.5 state (dashed line), and the perpetual-2090s RCP8.5 state (dotted line). We show regenerated oxygen,  $-TOU$ , to show the effect of utilization on  $O_2$  as additive. Note the nonlinear depth scale. (b) As (a) for the eastern tropical Atlantic. (The eastern tropical Pacific and Atlantic regions are defined in Fig. 4.)

477 In general terms, Figure 6 shows that the global decline in respiration acts toward  
 478 decreasing TOU (green bars; note that Fig. 6 shows  $\Delta O_2^{reg} = -\Delta TOU$ ), and hence in-  
 479 creasing  $O_2$  everywhere, as expected. Conversely, the slower 2090s circulation increases  
 480 TOU (blue bars) by increasing the upstream exposure time, allowing respiration, albeit  
 481 at a reduced rate, to act over longer times. The magnitude of the cross-term contribu-  
 482 tions to  $\Delta TOU$  (orange bars) are generally on the same order as the circulation-only and  
 483 respiration-only contributions, partly because of the large changes considered here. Note  
 484 that the  $\Delta TOU$  cross term acts toward increasing  $O_2$  because  $\Delta OUR$  and  $\Delta \Gamma_\Omega^\uparrow$  have op-  
 485 posite signs (negative contribution to  $\Delta TOU$ ). We now examine the drivers of TOU changes  
 486 in detail for the upper and deep ETP.

487 For the upper ETP (Fig. 6a,c), respiration-driven TOU reduction (green bar) is closely  
 488 compensated by circulation-driven TOU increases (blue bar). This shows that in the up-

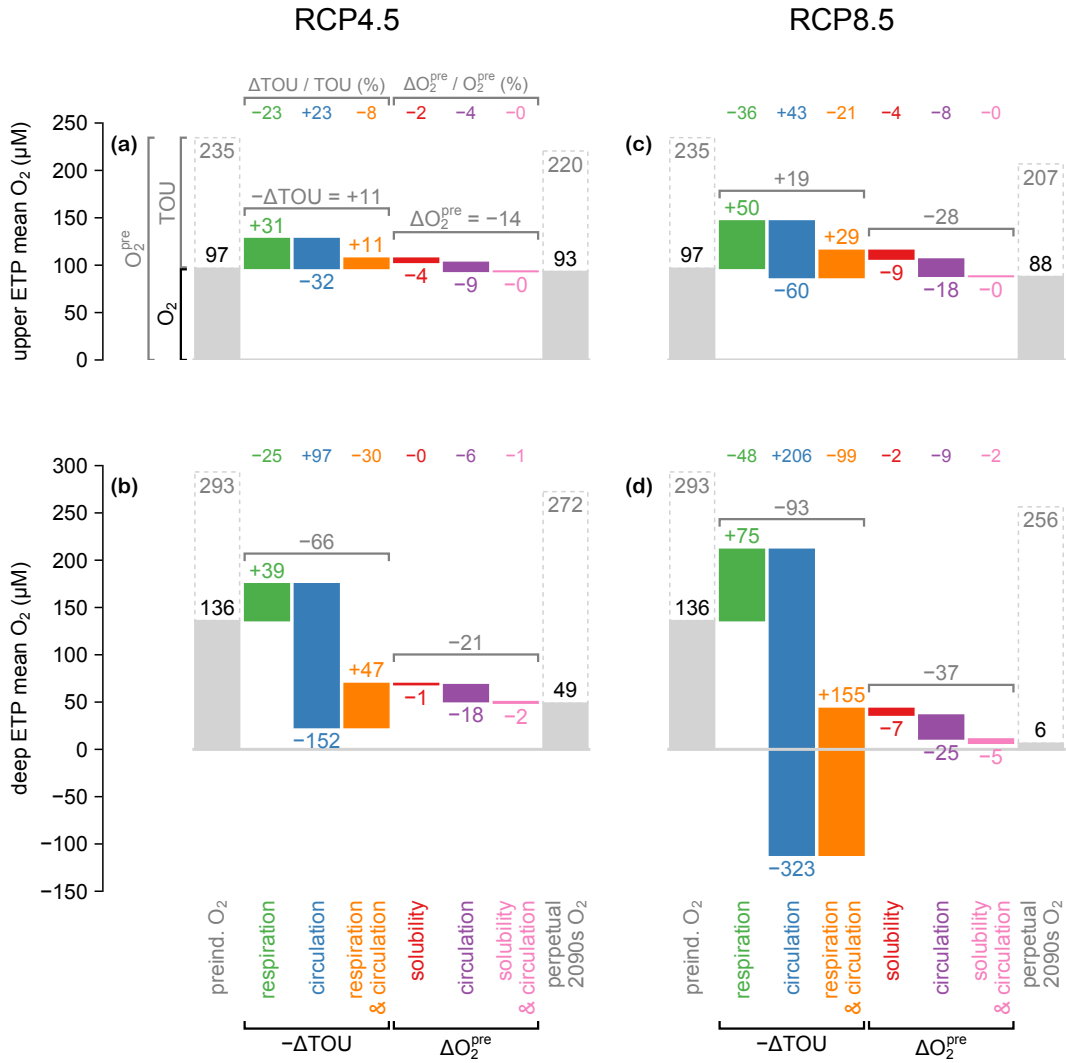


**Figure 6.** (a)  $\Delta O_2$  contributions for the upper ETP (0–500 m) for RCP4.5 plotted as a waterfall chart with the  $O_2$  change from the preindustrial state (leftmost gray bar) to the perpetual-2090s state (rightmost gray bar) decomposed into contributions (colored bars) that start where the previous one ends.  $\Delta TOU$  is decomposed according to Eq. (3) into contributions from changes in respiration (green), circulation (blue), and their spatial covariance (orange).  $\Delta O_2^{pre}$  is decomposed into contributions from solubility (red), circulation (purple), and their spatial covariance (pink). Percentage contributions to changes in  $TOU$  and  $O_2^{pre}$  are indicated at the top. (b) As (a) for the deep ETP (below 2000 m). (c–d) As (a–b) for RCP8.5.

per ocean respiration is slower (driving  $TOU$  reductions of 23% and 36% for RCP4.5 and RCP8.5), but the slower circulation allows this respiration to act for longer (driving  $TOU$  increases of 23% and 43%). As the effects of respiration-only changes (green

bars) and circulation-only changes (blue bars) nearly cancel, the overall TOU decrease is driven by the spatial correlation between respiration changes and circulation changes (orange bars). The concurrent increase of the circulation-only driven TOU and decrease of the respiration-only driven TOU must result in a negative cross term and hence in a TOU reduction, the precise magnitude of which depends on details of the underlying spatial patterns. The magnitude of the overall TOU decrease is about 8% for RCP4.5 and 21% for RCP8.5.

For the deep ETP, the circulation-only-driven  $\Delta$ TOU (blue bars) dominates the other drivers with a magnitude that is roughly 5 times larger than for the upper ETP. In comparison, the magnitude of the respiration-only-driven  $\Delta$ TOU (green bars) is only 30% and 50% larger for RCP4.5 and RCP8.5 than in the upper ETP. The respiration-driven decreases and circulation-driven increases in TOU again point to slower respiration acting for longer time. To quantify this, we calculated the upstream-exposure-time-weighted change in OUR and the OUR-weighted change in upstream exposure time to find that respiration slows by 25% for RCP4.5 and 50% for RCP8.5 but acts 2 times longer for RCP4.5 and 3 times longer for RCP8.5. For the deep ETP the cross terms (orange bars) are of the same order of magnitude as the respiration-only contribution (green bars), but the cross terms no longer dominate the overall TOU change as in the upper ETP. With all terms combined, the TOU of the deep ETP increases by 42% for RCP4.5 and by 59% for RCP8.5. A striking feature of these results is that, were respiration to be held constant at its preindustrial level, the  $\Delta$ TOU contribution from the circulation slowdown alone (blue bars) is so strong that it would have the potential to remove the entire  $O_2$  content of the deep ETP (filled gray bars) in the RCP4.5 scenario, and to do so more than two times over in the RCP8.5 scenario.

### 3.2.3 Upper and deep ETP budgets of $\Delta O_2^{\text{pre}}$

The preformed oxygen content of volume  $\Omega$  is controlled by euphotic  $O_2$  concentrations and by the amount of the  $\Omega$  volume that is ventilated per unit area at the base of the euphotic layer,  $V_\Omega^\downarrow$  (see Methods, Section 2, Eq. (4)). While  $V_\Omega^\downarrow$  depends only on the circulation, euphotic  $O_2$  concentration is determined by both solubility and circulation through the subtle balance between air-sea gas exchange and euphotic-zone residence time. However, decomposing euphotic  $O_2$  into saturation and disequilibrium components,  $O_2^{\text{sat}}$  and  $O_2^{\text{dis}}$ , allows us to separate solubility from circulation effects (includ-

524 ing their spatial correlation “cross term” in Eq. (5)) because euphotic  $O_2^{\text{sat}}$  is determined  
 525 by in situ solubility only, while euphotic  $O_2^{\text{dis}}$  is predominantly determined by circula-  
 526 tion. These contributions, volume integrated over either the upper or deep ETP, are also  
 527 plotted as colored bars in Fig. 6.

528 Reduced surface solubility reduces the preformed oxygen inventory of the ETP by  
 529 just a few percent (red bars) even for the extreme RCP8.5 case, accounting for less than  
 530 ~30 % of the overall  $O_2^{\text{pre}}$  decrease in the upper and deep ETP. The bulk (~70 % or more)  
 531 of the overall order-10 % decline in preformed oxygen is instead driven by changes in cir-  
 532 culation (purple bars). The cross terms (pink bars) between already relatively small solubility-  
 533 only and circulation-only contributions are essentially negligible. The circulation-only  
 534 driven reductions in  $O_2^{\text{pre}}$  due to  $\Delta\mathcal{V}_\Omega^\downarrow$  represent re-arrangements in euphotic origin be-  
 535 cause the area integral of  $\mathcal{V}_\Omega^\downarrow$ , which equals the volume of  $\Omega$ , is constant across all states.  
 536 The decreases in the circulation-only contributions to  $\Delta O_2^{\text{pre}}$  (computed with the prein-  
 537 dustrial surface oxygen concentration) thus indicate a shift in ventilation pattern toward  
 538 surface locations with lower oxygen concentration, i.e., toward warmer latitudes with lower  
 539 solubility (see also Appendix Fig. B4). This equatorward shift in ventilation reduces the  
 540 efficiency of the oxygen solubility pump and is the dominant driver of the decline in the  
 541 preformed  $O_2$  in both the upper and deep ETP.

542 It is interesting to note that regions with weaker ventilation have longer surface res-  
 543 idence time and thus higher surface saturation, which can compensate for reduced sol-  
 544 ubility. In our perpetual-2090s states this occurs near the Weddell and Ross seas where  
 545 the deep preindustrial mixed layer shoals dramatically thereby increasing surface resi-  
 546 dence and saturation, which overwhelm the effect of reduced solubility leading to increased  
 547 surface oxygen concentrations.

### 548   3.2.4 TOU changes in the ETP: three-dimensional distribution of TOU 549       origin

550 Having quantified the globally integrated drivers of ETP deoxygenation, we now  
 551 investigate their spatial distribution, beginning with the local contributions to TOU. The  
 552 local contribution at point  $\mathbf{r}$  to the TOU inventory of region  $\Omega$  is given by the product  
 553  $\Gamma_\Omega^\uparrow(\mathbf{r}) \text{OUR}(\mathbf{r})$ , which quantifies the origin of the TOU inventory, i.e., the oxygen loss  
 554 that occurred at  $\mathbf{r}$  upstream of  $\Omega$ . Figures 7 and 8 show the TOU origin for the upper

555 and deep ETP, respectively. The zonally integrated TOU origin is plotted for the prein-  
 556 dustrial state together with the corresponding changes for the perpetual-2090s states.

557 For the upper ETP (Fig. 7), TOU originates almost exclusively in the Pacific, pre-  
 558 dominantly in thermocline waters across all non-polar latitudes, with peak contributions  
 559 at a depth of  $\sim$ 200 m. Thus, there is significant oxygen loss within the upper-ocean cir-  
 560 culation as it transports oxygen to the upper ETP. TOU in the upper ETP also orig-  
 561 inates at depths between 1000–2000 m at low and high latitudes, where upwelling old oxy-  
 562 gen is intercepted by the bacterial respiration of abundant sinking organic matter be-  
 563 neath high productivity. For both RCP4.5 and RCP8.5, the change in TOU origin re-  
 564 veals a shoaling (upward shift) of the average location where oxygen bound for the up-  
 565 per ETP is lost. This shift presumably occurs because the slower 2090s circulation al-  
 566 lows respiration to act for longer so that oxygen bound for the upper ETP is stripped  
 567 out higher in the water column. The TOU origin below the thermocline at low and high  
 568 latitudes decreases, presumably because of reduced biological productivity and subja-  
 569 cent respiration, as well as a lower  $O_2$  content of the water that upwells there. The up-  
 570 ward shift in TOU origin and reduced deep origin are thus both consequences of respi-  
 571 ration removing oxygen sooner, i.e., further upstream, during its transit from the euphotic  
 572 zone.

573 For the deep ETP (Fig. 8), TOU originates in every ocean basin. The Atlantic makes  
 574 a 20 % contribution and the Indian Ocean a 15 % contribution, mostly at high latitudes  
 575 known to ventilate the deep Pacific (e.g., Holzer et al., 2021). For all basins, the largest  
 576 TOU origin lies in upper thermocline waters where most respiration occurs. Deeper TOU  
 577 origin at high latitudes, and in the Pacific throughout the water column at low latitudes,  
 578 occurs below regions of vigorous biological production where respiration is high. The fact  
 579 that the low-latitude tongue of oxygen loss in the Pacific lies partly above, and hence  
 580 *down-stream* of the deep ETP, implies that either some  $O_2$  is utilized as it mixes diffu-  
 581 sively downward, or, more likely, that water destined to be carried by meridional over-  
 582 turning back to the deep ETP at depth has its oxygen stripped out in the upwelling branch  
 583 of the overturning. Consistent with such an overturning pathway, local maxima of TOU  
 584 origin occur in the mid-depth North Pacific and in the abyssal Pacific sector of the South-  
 585 ern Ocean.

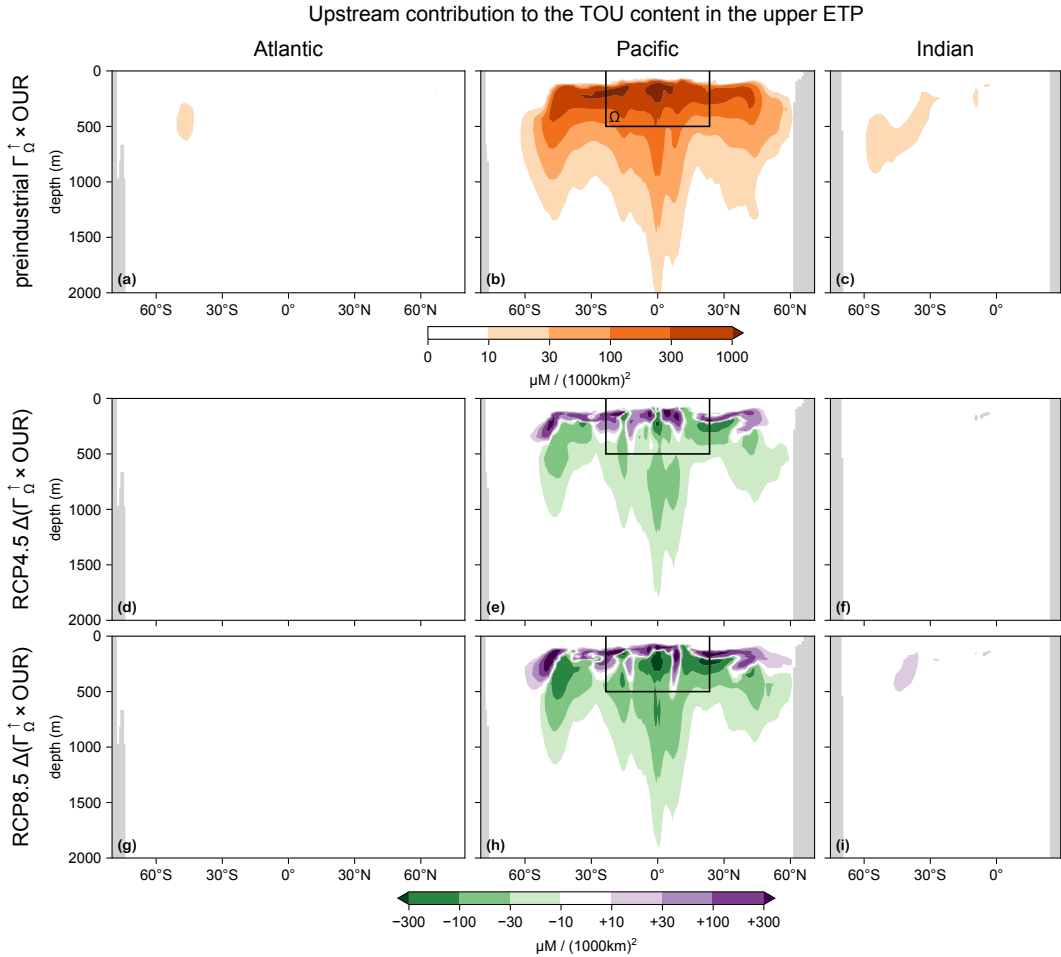


**Figure 7.** Preindustrial upstream contribution to the TOU in the upper ETP (0–500 m; indicated by the solid black line; subvolume  $\Omega$  in our equations) as quantified by basin zonal integrals of  $\Gamma_{\Omega}^{\uparrow} \times \text{OUR}$  normalized by the ETP volume for the Atlantic (a), Pacific (b), and Indian Ocean (c). (d–f) As (a–c) for the change from the preindustrial state to the perpetual-2090s state for the RCP4.5 scenario. (g–i) As (d–f) for RCP8.5. Note the nonlinear color scale and that the normalized zonal integrals plotted give the contribution per unit latitude–depth area.

The changes in the TOU origin of the deep ETP plotted in Fig. 8 show a global increase and upstream intensification of the removal of oxygen destined for the deep ETP. For the RCP4.5-based perpetual-2090s state, the TOU origin increases mostly near the surface of the Pacific, South Atlantic, and southern Indian Ocean where it was already large in the preindustrial state. For RCP8.5, the TOU contributions are generally stronger and, unlike for RCP4.5, they also increase near the North Atlantic surface. However, in the old waters of the mid-depth North Pacific the TOU origin of the deep ETP actually

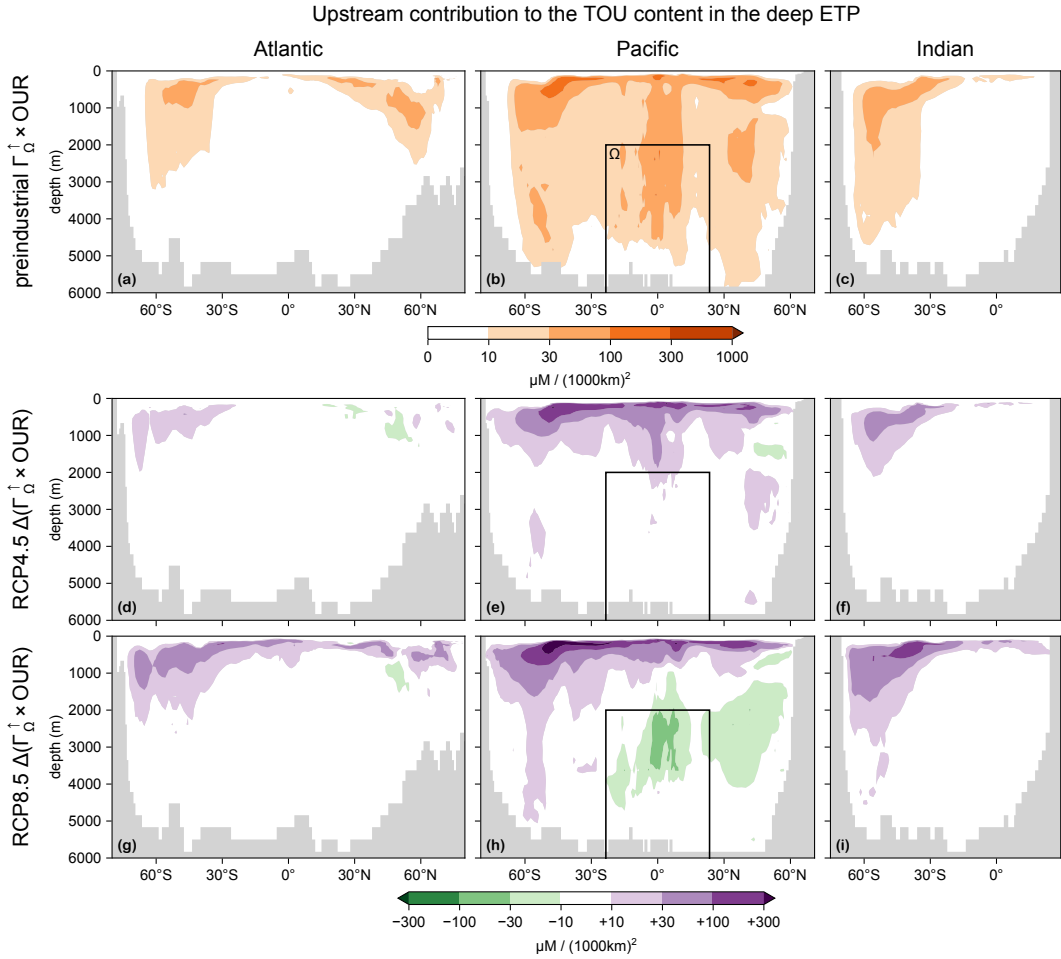


**Figure 8.** As Fig. 7 for the deep ETP (below 2000 m; indicated by the solid black line).

decreases for RCP8.5, likely because of shifts in production, and hence respiration, away from the surface origin of these old waters so that less oxygen is stripped out of them.

593           **3.2.5 Preformed oxygen changes in the ETP: shifting ventilation pat-**  
 594           **terns**

597         Here we take a closer look at the geographic shifts in ventilation patterns that drive  
 598         the decreased preformed oxygen content of the ETP. The amount of  $\text{O}_2^{\text{pre}}$  supplied to  $\Omega$   
 599         from euphotic location  $r$  is quantified by the product  $\text{O}_2(r) \mathcal{V}_\Omega^\downarrow(r)$ , maps and zonal in-  
 600         tegrals of which are plotted in Fig. 9 for the preindustrial state together with the changes  
 601         for the perpetual-2090s states. (Corresponding plots of  $\mathcal{V}_\Omega^\downarrow$  by itself, shown in Appendix  
 602         Fig. B4, share strong similarities with Fig. 9, underscoring that changes in ventilation pat-  
 603         terns are the dominant driver of  $\Delta\text{O}_2^{\text{pre}}$ .)

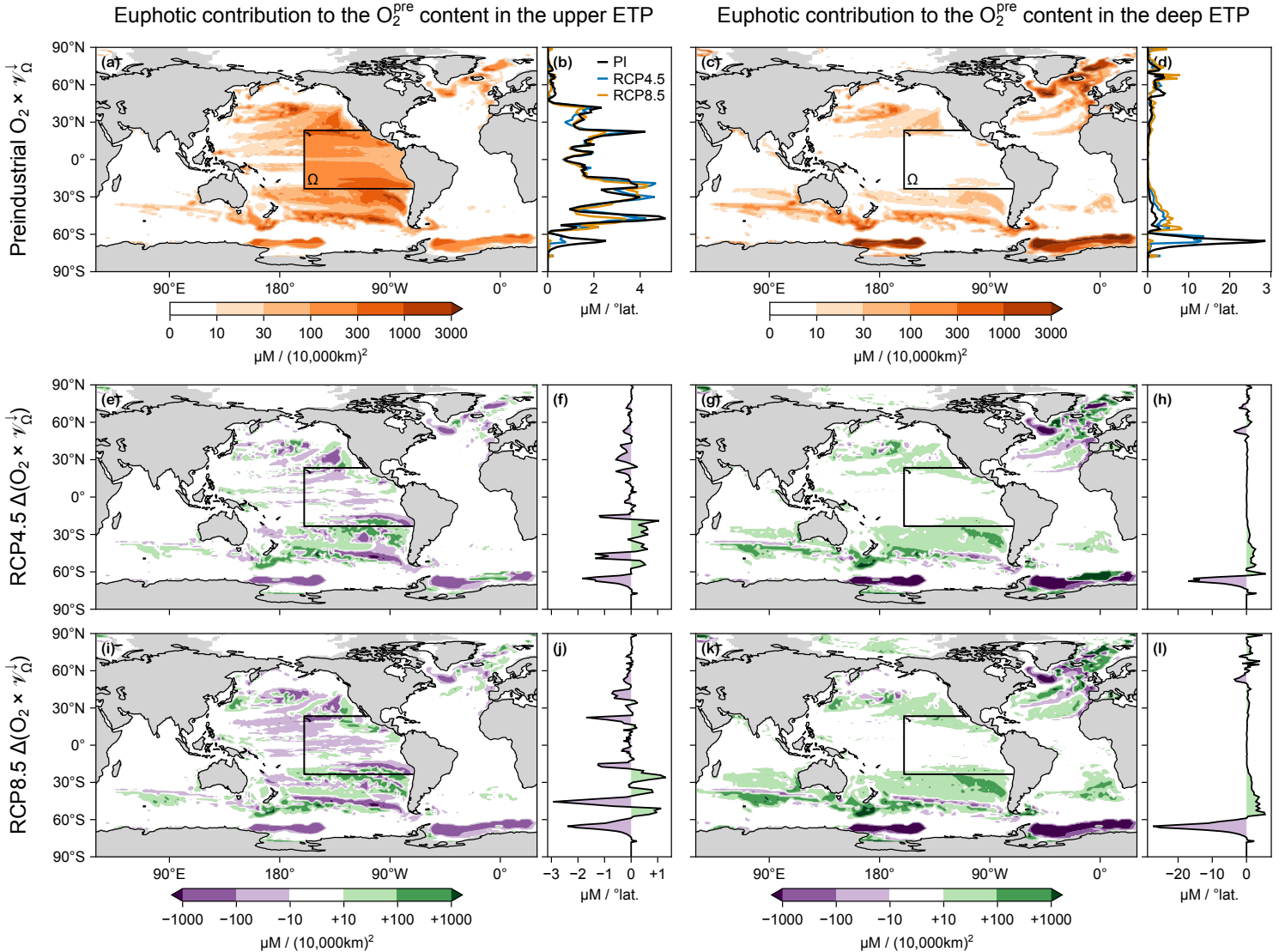


**Figure 9.** (a) Map and (b) zonal integral of the euphotic contribution to the mean  $O_2^{\text{pre}}$  in the upper ETP (subvolume  $\Omega$  indicated by a solid black contour), as quantified by  $O_2 \times \mathcal{V}_\Omega^\downarrow$  normalized by the volume of  $\Omega$ , in the preindustrial state. (c–d) As (a–b) for  $\Omega$  the deep ETP. (e–h) As (a–d) for  $\Delta(O_2^{\text{pre}} \times \mathcal{V}_\Omega^\downarrow)$  for the RCP4.5 perpetual 2090s. (i–l) As (e–h) for RCP8.5. Note the nonlinear color scale and that the contributions plotted are per unit horizontal area.

604 For the upper ETP, the origin of preformed oxygen in the preindustrial state (Fig. 9a)  
 605 shows that while much oxygen comes from the overlying surface, a considerable fraction  
 606 is supplied from Mode and Intermediate water-formation regions in the Pacific, and from  
 607 deep-water formation regions in the Southern Ocean (Weddell and Ross Seas) and North  
 608 Atlantic. For the deep ETP in the preindustrial state, the tropical and subtropical con-  
 609 tributions are much weaker while contributions from the deep-water formation regions  
 610 of the Southern Ocean and the North Atlantic are more important.

611 For the perpetual-2090s states, the largest decreases in preformed oxygen origin  
 612 occur in the deep-water formation regions, particularly near the Weddell and Ross Seas.  
 613 The supply of  $O_2^{pre}$  from south of 60°S declines by about 70 % and 50 % for the upper  
 614 and deep ETP, respectively, for the RCP4.5 scenario, and almost completely shuts down  
 615 for both the upper and deep ETP for RCP8.5. As discussed for Fig. 6 and underscored  
 616 by the similarity between Fig. 9 and Appendix Fig. B4, this is dominantly due to circulation-  
 617 driven changes in ventilation. Large-scale increases of the  $O_2^{pre}$  supply are most promi-  
 618 nent in the subtropical gyres, which are more important oxygen sources for the ETP in  
 619 our perpetual-2090s states.

## 620 4 Discussion

621 We investigated the deoxygenation of the ocean for idealized steady-state biogeo-  
 622 chemistry in equilibrium with frozen-in-time physical ocean states. We used two ocean  
 623 states averaged over the 2090s for the RCP4.5 and RCP8.5 scenarios and held constant  
 624 in time for perpetuity, plus a corresponding 1990s steady state (“preindustrial” for short)  
 625 for our analysis. To attribute the deoxygenation to its drivers, we focused on the east-  
 626 ern tropical basins (primarily in the Pacific) as these contain OMZs in the current ocean,  
 627 and because their deoxygenation is typical of the large-scale steady-state response in our  
 628 model. The key driving mechanisms were quantified by decomposing the oxygen changes  
 629 into contributions from changes in surface solubility, ocean circulation, and oxygen uti-  
 630 lization rates. Here we discuss important caveats of our approach and contrast our re-  
 631 sults with other work on ocean deoxygenation.

632        **4.1 Caveats**

633        A number of caveats must be kept in mind when interpreting our findings. Some  
 634        caveats also apply to the nutrient and carbon cycles and have been previously discussed  
 635        by Pasquier et al. (2023, 2024). Below we discuss the caveats specific to our analysis of  
 636        deoxygenation.

637        (i) The biogeochemical states analyzed here are steady and embedded in circulations that  
 638        are frozen in time. By contrast, the real ocean circulation is currently slowing down and  
 639        will continue to evolve for millennia even for fixed external forcing (e.g., Srokosz & Bry-  
 640        den, 2015). Given the ocean's wide range of transit times (e.g., Primeau, 2005), the cir-  
 641        culation will keep changing well beyond the 21st century until deep convection, venti-  
 642        lation, and overturning eventually recover after a few millennia (e.g., Schmittner et al.,  
 643        2008), which results in a different state from those considered here. Thus, neither the  
 644        oxygen distribution nor the circulation and thermodynamic ocean state are expected to  
 645        be anywhere near steady by the end of the 21st century (e.g., Shaffer et al., 2009). Our  
 646        biogeochemical states therefore cannot be interpreted as predictions of the future. In par-  
 647        ticular, by allowing oxygen to fully equilibrate with frozen circulations that feature strongly  
 648        weakened Southern Ocean ventilation and bottom-water formation, our idealized steady  
 649        states exhibit intense abyssal deoxygenation that will certainly not be manifest by 2100.  
 650        However, our analysis does provide a glimpse into the possible mechanisms that could  
 651        shape the oxygen response on its very longest timescales. Furthermore, our steady-state  
 652        framework accounts for neither natural variability nor seasonality. In particular, we can-  
 653        not capture the effects from seasonally covarying changes in biology, physics, and ther-  
 654        modynamics, which play a significant role in the seasonality of oxygen in the upper few  
 655        hundred meters as seen in both observations and models (see, e.g., Jin et al., 2007; Graco  
 656        et al., 2017; Espinoza-Morriberón et al., 2021; Pitcher et al., 2021, to cite a few).

657        (ii) In terms of precise quantitative values, our results are specific to the circulation of  
 658        the parent climate model. The unrealistically deep Southern Ocean mixed layer of the  
 659        preindustrial state inherited from the parent ACCESS1.3 model (Bi et al., 2013), and  
 660        its shoaling in the future, leave a pronounced imprint on our results. However, unreal-  
 661        istically deep mixed layers in the polar Southern Ocean are a feature common to virtu-  
 662        ally all CMIP5 models (e.g., de Lavergne et al., 2014), in which AABW is formed by deep  
 663        convection compensating for unresolved sinking of Antarctic shelf waters. Importantly,

the qualitative deoxygenation mechanisms identified here for idealized steady-state oxygen in frozen-in-time 2090s circulation are unlikely to depend on which particular CMIP5 model is used to generate the idealized state. Most CMIP5 models share the qualitative feature of declining Southern Ocean ventilation and shoaled mixed layers at the end of the 21st century (e.g., de Lavergne et al., 2014; Heuzé et al., 2015; Kwiatkowski et al., 2020). These are both critical circulation changes for producing intense equilibrated deoxygenation when the circulation is frozen in time. Another relevant feature of the ACCES1.3 parent model is that it does not include melting land-fast ice sheets, which impact Southern Ocean ventilation (Li et al., 2023; Chen et al., 2023). If meltwater from ice sheets were included, we would expect a stronger reduction in Southern Ocean ventilation (Purich et al., 2018; Purich & England, 2023), which we would expect to strengthen the circulation-change contribution to deoxygenation. We emphasize, however, that accurate circulation changes with detailed realism are not important for our idealized deoxygenation scenarios. Any circulation with reduced Southern Ocean ventilation and throttled bottom-water formation that is frozen in time is likely to produce intense abyssal deoxygenation similar to what we document here.

(iii) In terms of quantitative detail, our results are also specific to the PCO<sub>2</sub> biogeochemistry model that was used (Pasquier et al., 2023). PCO<sub>2</sub> was designed to be relatively simple and does not explicitly represent every mechanism at play in the real ocean. Potentially important missing mechanisms include feedbacks from the nitrogen cycle, which are linked to oxygen through denitrification and nitrification. Denitrification, which is only modelled implicitly in PCO<sub>2</sub> (see Methods, Eq. (1)), is important because anaerobic respiration in low oxygen environments acts as an effective oxygen source. Conversely, nitrogen fixation and nitrification, which produce nitrite and nitrate by consuming oxygen, are not represented at all in PCO<sub>2</sub>. Effects from the nitrification–denitrification imbalance on the oxygen cycle, expected to contribute about two thirds of a ~6 % increase in the global O<sub>2</sub> inventory by the year 8000 (Oschlies et al., 2019), are therefore not captured in our model. However, we note that this imbalance is expected to be dominated by denitrification (which is parameterized in PCO<sub>2</sub>) and remains secondary for the first few centuries of sluggish circulation until about the year 5000 when the overturning circulation recovers.

695        **4.2 Relation to previous work**

696        Because our analysis is framed for idealized steady-state biogeochemistry in equi-  
697        librium with frozen-in-time circulations, we do not expect a detailed match with previ-  
698        ous studies based on transient simulations. We do, however, expect similarities with sim-  
699        ulations that last long enough for the effect from slow processes to manifest. In partic-  
700        ular, this includes processes mediated by the slowdown of the deep ocean circulation, which  
701        is the dominant driver of deoxygenation in our analyses and operates on multi-centennial  
702        timescales (e.g., Primeau, 2005), with effects that will not have asserted themselves by  
703        the end of the 21st century in transient simulations of oxygen (e.g., Moore et al., 2018).  
704        However, the relatively more sluggish ocean state predicted for the next few centuries  
705        will likely only be temporary. A more vigorous circulation is expected to return after sev-  
706        eral millennia as deep ocean temperatures equilibrate (e.g., Schmittner et al., 2008; Frölicher  
707        et al., 2020). The more vigorous circulation and stronger Southern Ocean ventilation pre-  
708        dicted for a future steady state of the ocean could thus result in the opposite response  
709        found here for our perpetually warmer and slower ocean states. In particular, in the very  
710        long term, deep preformed O<sub>2</sub> could actually increase despite a globally warmer ocean  
711        because of a poleward shift in the origin of deep oxygen. We therefore expect our results  
712        to be most relevant to predictions for a few centuries into the future before a more vig-  
713        orous circulation re-establishes. We also note that differences in biogeochemistry, in ocean  
714        circulation, in scenarios and forcings, and so on, further complicate quantitative com-  
715        parisons.

716        The very intense deoxygenation seen here at depth is driven by circulation changes  
717        that act in perpetuity, while corresponding effects in transient simulations have not fully  
718        developed by 2100. Thus, our results on deoxygenation are generally different in mag-  
719        nitude from what is seen in transient simulations, with very dramatic differences in the  
720        deep ocean. For the upper ocean, Kwiatkowski et al. (2020) reported a  $(10 \pm 2)\%$  de-  
721        cline in 100–600 m deep oxygen across CMIP5 models and a  $(13 \pm 5)\%$  decline across  
722        CMIP6 models for RCP8.5 and SSP5-8.5, respectively, compared to the  $\sim 20\%$  decline  
723        for our RCP8.5-based perpetual-2090s steady state. (CMIP6 uses the “Shared Socio-  
724        economic Pathway” (SSP) classification (Riahi et al., 2017) where SSP5-8.5 nominally matches  
725        RCP8.5 (Arias et al., 2021).) Similarly, for RCP4.5, Kwiatkowski et al. (2020) reported  
726        a  $6 \pm 3\%$  decline for CMIP5 and a  $8 \pm 4\%$  decline for CMIP6, compared to a  $\sim 7\%$  de-  
727        cline in this study for the same scenario. Near the sea floor, Kwiatkowski et al. (2020)

728 reported a weak but consistent  $6 \pm 2\%$  oxygen decline across CMIP6 models and sce-  
 729 narios, in stark contrast to the  $\sim 40\%$  and  $\sim 80\%$  decline in the abyss for our RCP4.5-  
 730 and RCP8.5-based states, respectively. The hypoxic volumes in our perpetual-2090s states  
 731 are thus dramatically larger than the predictions of a moderate  $\sim 10\%$  expansion in mild  
 732 hypoxia and a contraction of the OMZ core (e.g., Gnanadesikan et al., 2012; Busecke et  
 733 al., 2022).

734 Longer-term transient simulations in principle allow for closer comparisons with  
 735 our steady-state biogeochemistry embedded in frozen-in-time circulations but the recov-  
 736 ery of the transient ocean circulation intervenes before the long-term effects of circula-  
 737 tion slowdown can fully develop. Running a climate model with  $p\text{CO}_2$  at three times its  
 738 preindustrial level from 2100 onward, Matear and Hirst (2003) reported a  $\sim 30\%$  decline  
 739 in  $\text{O}_2$  below 4000 m by 2700. This  $\text{O}_2$  decline is larger than those estimated for 2100 but  
 740 still far from the corresponding 80 % decline of our RCP8.5 perpetual-2090s state because  
 741 the circulation effects on  $\text{O}_2$  are not fully developed as evidenced by a deep  $\text{O}_2$  trend that  
 742 remains strongly negative by 2700. Matear and Hirst (2003) report spatial patterns that  
 743 are similar to our steady-state responses, with intense  $\text{O}_2$  declines in the deep Southern  
 744 Ocean driven by decreased ventilation. However, the simulation by Matear and Hirst (2003)  
 745 was not continued beyond 2700, which is roughly when the circulation is expected to start  
 746 recovering. In a multimillennial double- $p\text{CO}_2$  simulation, Frölicher et al. (2020) find a  
 747 700-yr decline in  $\text{O}_2$  mostly below 2000 m accumulating to a  $\sim 10\%$  loss globally (com-  
 748 pared to 40 % for our RCP4.5 perpetual-2090s state) before  $\text{O}_2$  slowly increases again  
 749 over multiple millennia driven by the recovery of Southern-Ocean ventilation. In another  
 750 multimillennial simulation with atmospheric  $p\text{CO}_2$  reaching almost 2000  $\mu\text{atm}$  around  
 751 year 2300 and slowly declining to  $\sim 1200 \mu\text{atm}$  over the next five millennia, Oschlies et  
 752 al. (2019) find an  $\text{O}_2$  decline of  $\sim 25\%$ , also reached around year 2700, before  $\text{O}_2$  levels  
 753 increase again with the recovering overturning circulation.

754 Our analyses differ from previous studies by attributing deoxygenation to specific  
 755 mechanisms, in particular by cleanly separating out the role of circulation changes. In  
 756 our work here, solubility alone accounts for less than 10 % of the global  $\text{O}_2$  decline, which  
 757 is lower than what is estimated for the transient 2100 ocean. Its idealized framework notwith-  
 758 standing, our analysis of the role of solubility changes suggests that previous studies po-  
 759 tentially overestimate the solubility contribution. Studies that infer the solubility con-  
 760 tribution from a residual, typically between a climate-change simulation and a similar

simulation with the solubility fixed to preindustrial values (e.g., Matear & Hirst, 2003), unintentionally include effects from changes in ventilation patterns (which should be attributed to circulation change) because the residual includes spatial correlation (“cross”) terms, which we estimate to be order 20 % for our steady states in frozen-in-time circulations. Approximations based on heat flux generally overestimate the contribution from solubility changes because they assume complete saturation (e.g., 20–30 %; Bopp et al., 2002; Palter & Trossman, 2018). Solubility-change contributions quantified through an abiotic/preformed O<sub>2</sub> tracer are generally overestimated yet more (e.g., 30–50 %; Oschlies et al., 2019; Oschlies, 2021) because the preformed tracers respond to both saturation and circulation changes. Similarly, solubility contributions quantified directly by the change in saturation concentration as a function of in situ temperature and salinity are overestimated even more (e.g., 40–70 %; Frölicher et al., 2020). Only studies that perturb surface solubility alone in an otherwise unperturbed preindustrial state can provide unbiased estimates. Such unbiased estimates include, e.g., the 15 %, 25 %, and 35 % estimates by Matear et al. (2000), Bopp et al. (2002), and Plattner et al. (2001), respectively, the higher estimates likely being due to models with smaller changes in Southern Ocean ventilation.

## 5 Conclusions

We quantified the drivers of large-scale ocean deoxygenation for idealized steady-state biogeochemistry embedded in perpetual-2090s ocean states based on RCP4.5 and RCP8.5 ACCESS1.3 simulations. Our analysis is idealized because we allowed oxygen to fully equilibrate with a perpetually warmer and slower ocean, which is in stark contrast to transiently evolving biogeochemistry embedded in a more realistic dynamically changing circulation. Changes in biogeochemistry were evaluated relative to a steady preindustrial state and analyzed for the eastern tropical Pacific (ETP), which contains the largest hypoxic volume. We partitioned changes in TOU and preformed oxygen into their drivers, i.e., into contributions from changes in circulation, respiration, solubility, and their interactions (cross terms).

To quantify the drivers of deoxygenation, we employed novel diagnostic methods that leveraged the steady-state nature of our idealized biogeochemistry. Key to our being able to isolate — for the first time — the role of circulation changes in driving deoxygenation is the conceptually novel upstream exposure time, a circulation timescale

793 that controls the oxygen deficit of a given subvolume  $\Omega$  of the ocean. Specifically, it is  
 794 the time for which the oxygen that is “missing” from  $\Omega$  was exposed to upstream res-  
 795piration. The upstream exposure time thus provides the precise connection between TOU  
 796 and OUR (Holzer, 2022) and, as shown here, the precise link between ventilation vol-  
 797ume and preformed oxygen. In essence, the upstream exposure time, which is a function  
 798 of advective–diffusive transport, traces TOU and preformed oxygen back in time to their  
 799 origin.

800 Our main conclusions are as follows:

- 801 1. Keeping the 2090s ocean state frozen in time leads to steady-state oxygen distri-  
 802 butions characterized by intense global-scale deoxygenation at depth. Global oxy-  
 803 gen inventories decline by 30 % and 60 % for the RCP4.5 and RCP8.5 scenarios,  
 804 respectively. For the extreme RCP8.5 case, Pacific abyssal waters become severely  
 805 hypoxic ( $pO_2 \leq 15 \mu\text{M}$ ) over the entire basin, while Atlantic and Indian Ocean  
 806 abyssal waters become mildly hypoxic ( $pO_2 \leq 100 \mu\text{M}$ ) everywhere. The extent  
 807 of hypoxic regions in the upper ocean changes remarkably little in our more poorly  
 808 ventilated perpetual-2090s states, owing to decreased preformed oxygen being com-  
 809 pensated by reduced TOU.
- 810 2. For our idealized steady states, intense abyssal TOU increases are dominantly driven  
 811 by the perpetual 2090s circulation being slower, thus allowing respiration to act  
 812 over longer times. Modest upper-ocean TOU decreases are characterized by close  
 813 compensation between respiration-only and circulation-only effects. Specifically,  
 814 in the deep ETP, TOU increases of 50 % for RCP4.5 and 100 % for RCP8.5 are  
 815 driven by 2–3 times longer upstream exposure to respiration, which overwhelms  
 816 the decline in respiration rates. In the upper ETP, TOU decreases by about 10 %.  
 817 Thus, despite the global decline in respiration rates, the permanently slower cir-  
 818 culation of our idealized states drives intense deoxygenation at depth and prevents  
 819 increased oxygenation in the upper ocean.
- 820 3. In our idealized perpetual-2090s states, preformed oxygen declines virtually ev-  
 821 erywhere driven mostly by shifts in ventilation patterns, rather than by the de-  
 822 crease in solubility due to warmer sea-surface temperatures. More than 70 % of  
 823 the decline in preformed oxygen is driven by its surface origin shifting away from  
 824 high latitudes toward lower latitudes, where warmer waters hold less oxygen. In

situ warming-driven solubility reductions by themselves, at fixed circulation, reduce preformed oxygen by only  $\sim 30\%$  in the upper ETP and by less than  $20\%$  in the deep ETP, accounting for less than  $10\%$  of the overall deoxygenation. Thus, while preformed oxygen is often thought to decrease because of warming-driven reduced solubility (e.g., Palter & Trossman, 2018; Oschlies et al., 2019; Couespel et al., 2019; Oschlies, 2021), our analysis reveals that, at least when the 2090s ocean state is maintained in perpetuity, the change in ventilation pathways is the dominant driver.

Our results show that, for our idealized states, circulation change is the key driver of deoxygenation. What the precise contribution of circulation change will be in the future ocean remains an open question. Our analysis suggests that to understand the fate of oxygen in the ocean, it is important to carefully quantify ventilation patterns and key ocean circulation timescales. Of particular importance is the upstream exposure time which is a key control on both preformed oxygen and TOU. For steady state, the necessary computations can efficiently be performed by building and using the associated transport matrices as was done here, and which we hope will become a more widely adopted practice. For time-evolving states, the analysis becomes significantly more complex, and extending our work to a dynamically changing oxygen cycle is left to the future.

843 **Appendix A Model–observations comparisons**

844 Figure A1 shows the basin zonal-mean  $pO_2$  for the preindustrial state of our model  
 845 and for the GLODAPv2 observations, along with the corresponding mismatch. The un-  
 846 realistically deep mixed layers of the Southern Ocean in the parent model manifest as  
 847 overestimated  $pO_2$  in the Atlantic and Pacific south of 60°S. Other systematic model bi-  
 848 ases are visible, for example in the northern Indian Ocean, where PCO2 overestimates  
 849  $pO_2$ , and in the tropical and subtropical upper Atlantic and Pacific, where PCO2 un-  
 850 derestimates  $pO_2$ .

851 Figure A2 shows the areal extent of each hypoxia category in each ocean basin as  
 852 modelled for the preindustrial state and as captured by the GLODAPv2 observations.  
 853 The extent of the Atlantic and Pacific hypoxic areas is generally overestimated, while  
 854 the extent of the Indian-Ocean hypoxic areas is generally underestimated particularly  
 855 at depth, consistent with Fig. A1. We note that the  $pO_2$  thresholds used are different  
 856 for model and observations as they were adjusted for the model so that the global hy-  
 857 poxic volume for a given category is the same for the model as for GLODAPv2 (Meth-  
 858 ods, Section 2.6). (Note that the global match does not guarantee matching volumes within  
 859 a given basin.)

860 Figure A3 shows the geographic distribution of hypoxic waters as quantified by the  
 861 water-column minimum of  $pO_2$  for the preindustrial model state and for the GLODAPv2  
 862 observations. While the large-scale patterns seen in the observations are captured by the  
 863 model, there are significant mismatches. The underestimated  $pO_2$  in the Pacific and At-  
 864 lantic manifest as OMZs (hypoxia category C) that are larger than observed. The model  
 865 places the Indian Ocean OMZ southeast of western Indonesia while observations show  
 866 it to occur in the Bay of Bengal and in the Arabian Sea.

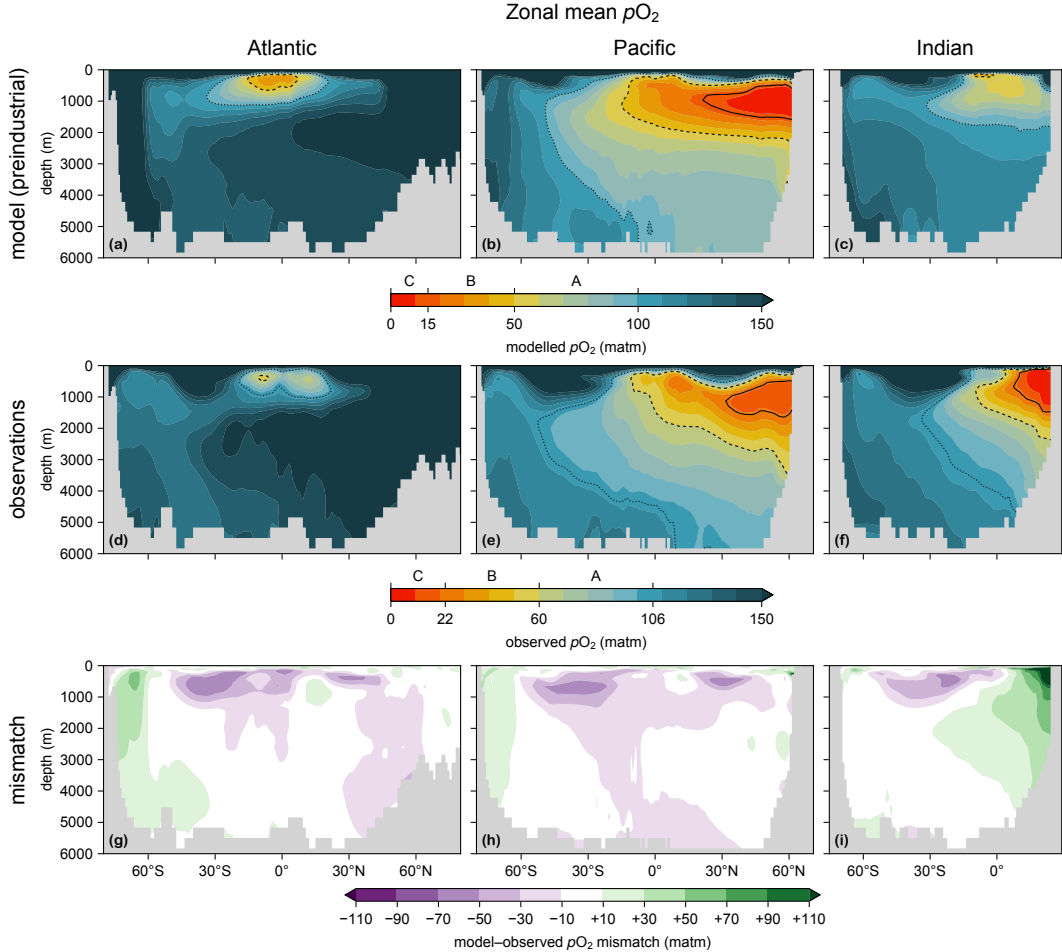


**Figure A1.** (a) Atlantic, (b) Pacific, and (c) Indian Ocean zonal mean  $p\text{O}_2$  for the preindustrial state. The dotted, dashed, and solid contour lines indicate the thresholds of hypoxia categories A, B, and C, respectively (which are different for model and observations; see Methods, Section 2.6). (d–f) As (a–c) for observations. (g–i) As (a–c) for the model–observations mismatch. The Atlantic basin excludes the Gulf of Mexico and the Caribbean, and the Pacific basin excludes the Sea of Japan so that the zonal means are more cleanly interpretable.

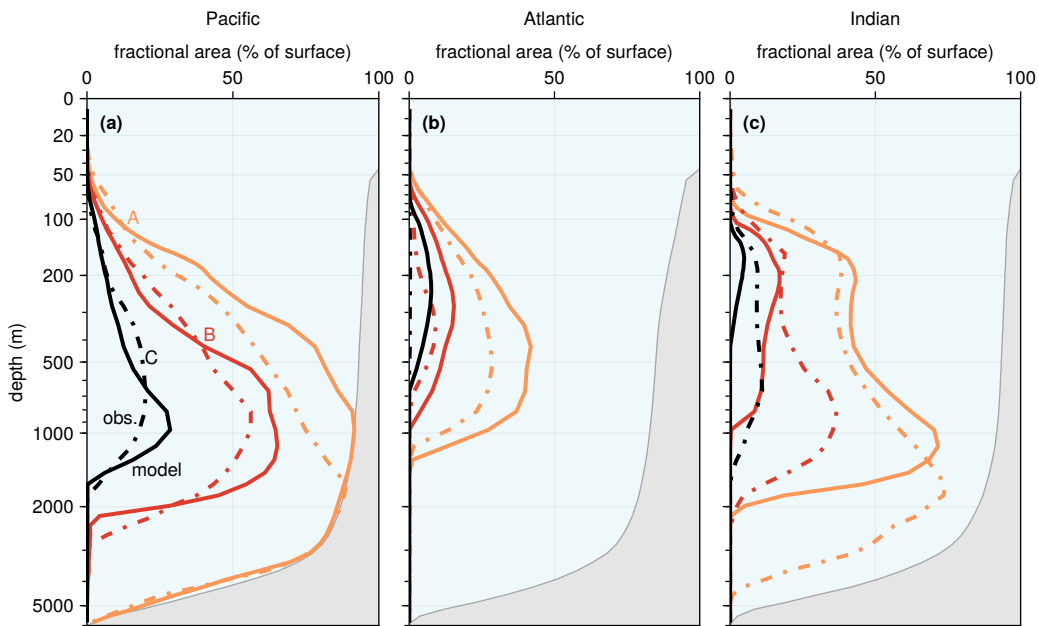


**Figure A2.** (a) Pacific depth profiles of the spatial extent of mild (A, orange), intermediate (B, red), and severe hypoxia (C, black) for the modelled preindustrial state (model; solid lines) and the observations (obs.; dash-dotted lines). (b) As (a) for the Atlantic. (c) As (a) for the Indian Ocean. (The gray shading represents the seafloor.) Note the nonlinear depth scale and that the  $p\text{O}_2$  thresholds used for model and observations are different (see Methods, Section 2.6).

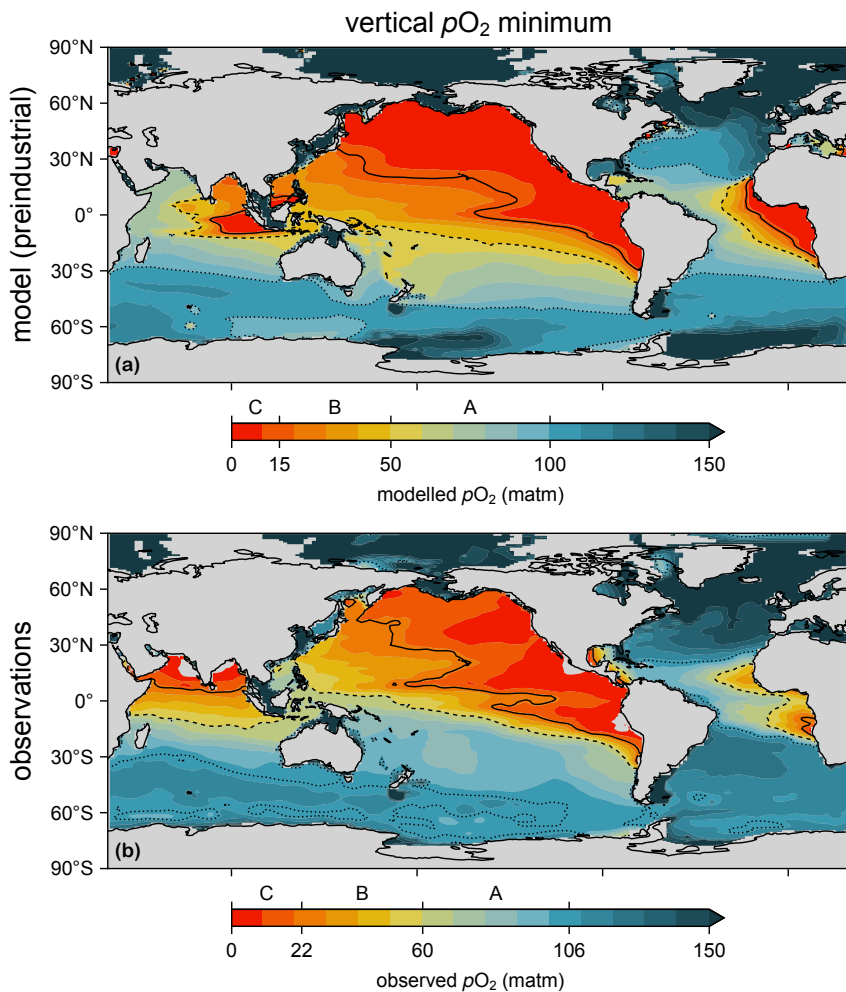


**Figure A3.** (a–b) Maps of the water-column minimum  $p\text{O}_2$  for (a) the modelled preindustrial state and (b) observations. The dotted, dashed, and solid contour lines indicate the thresholds of hypoxia categories A, B, and C, respectively (which are different for model and observations; see Methods, Section 2.6).

867 **Appendix B TOU and  $O_2^{\text{pre}}$ : patterns and drivers**

868 The left plots of Fig. B1 show the Pacific zonal mean  $O_2^{\text{pre}}$  for the preindustrial state  
 869 and the corresponding changes for the perpetual-2090s states. Near the surface,  $O_2^{\text{pre}}$  is  
 870 higher in cold waters with greater oxygen solubility, and in the interior  $O_2$  traces out (wa-  
 871 ter) ventilation pathways. In the perpetual-2090s states, preformed  $O_2$  declines almost  
 872 everywhere and more strongly at depth, except in the surface Southern Ocean above  $\sim 200$  m.

873 The right plots of Fig. B1 show zonal mean TOU, which increases progressively as  
 874 water traverses sinking organic matter where respiration strips out oxygen. TOU is gen-  
 875 erally largest at depths of about 500–1500 m in the preindustrial state, and increases sig-  
 876 nificantly at depth in the perpetual-2090s states. TOU and its changes are governed by  
 877 both oxygen utilization rates (OUR) and upstream sweeping times, shown below.

878 OUR, shown in the left plots of Fig. B2, is generally surface intensified by several  
 879 orders of magnitude as OUR is tightly linked to nutrient and carbon remineralization  
 880 which attenuates quickly with depth. In our perpetual-2090s states, biological produc-  
 881 tion and OUR decline globally though they are some local increases, mostly owing to spa-  
 882 tial shifts in the nutrient supply. However, the effect of changes in OUR on  $O_2$  is mod-  
 883 ulated by the time over which oxygen is exposed to respiration, discussed next.

884 The zonal-mean upstream exposure time  $\Gamma_\Omega^\uparrow(\mathbf{r})$  is shown in Fig. B2 for the case where  
 885 the interior volume  $\Omega$  of interest is either the upper ETP (middle plots) or deep ETP  
 886 (right plots). Because in steady state the upstream exposure time is also  $\Gamma_\Omega^\uparrow(\mathbf{r})$ , the time  
 887 that water at  $\mathbf{r}$  will spend in  $\Omega$ , its magnitude approximately scales with the volume of  
 888  $\Omega$ . Furthermore, because the deep circulation is much more sluggish than in the wind-  
 889 driven thermocline, upstream exposure times are shorter for the upper ETP (less than  
 890  $\sim 20$  years) than for the deep ETP (up to  $\sim 450$  years).  $\Gamma_\Omega^\uparrow$  is generally larger close to  
 891  $\Omega$  and decreases with distance from  $\Omega$ . Qualitatively,  $\Gamma_\Omega^\uparrow$  can be thought of as path se-  
 892 lector roughly akin to the concentration of fluid elements destined to pass through  $\Omega$  be-  
 893 fore exposure to the euphotic zone. Thus,  $\Gamma_\Omega^\uparrow$  is shorter further away from  $\Omega$  because more  
 894 of the water there will be reexposed to the euphotic zone before it has a chance to pass  
 895 through  $\Omega$ .

896 In the perpetual-2090s states, a slower circulation tends to increase  $\Gamma_\Omega^\uparrow$ , but altered  
 897 ventilation pathways can also reduce  $\Gamma_\Omega^\uparrow$  (lower middle and right plots of Fig. B2). For

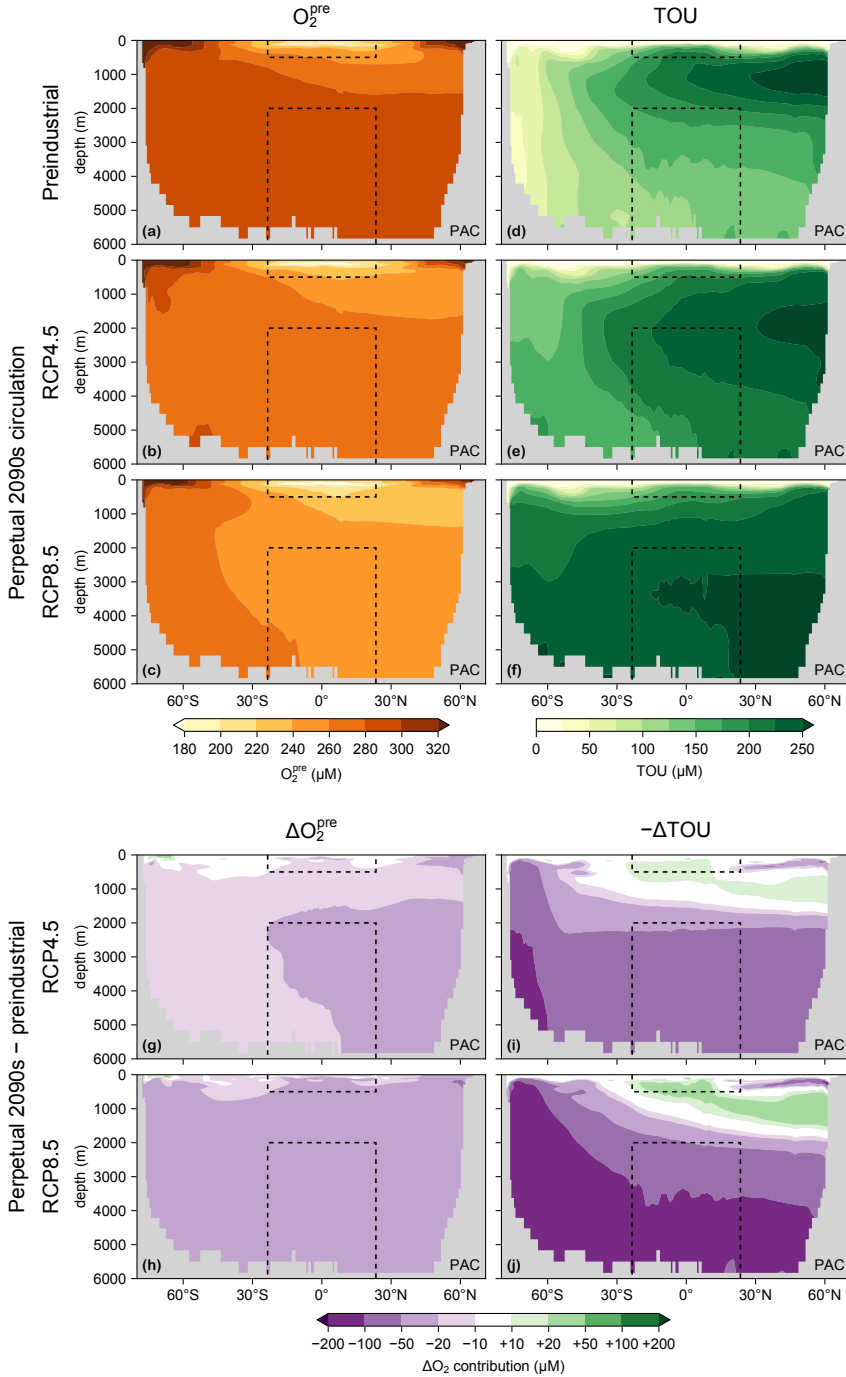


**Figure B1.** (a) Pacific zonal mean  $O_2^{\text{pre}}$  for the preindustrial state. (b–c) As (a) for the perpetual-2090s states (based on RCP4.5 and RCP8.5). (d–f) As (a–c) for TOU. (g–j)  $\Delta O_2^{\text{pre}}$  and  $\Delta \text{TOU}$  for RCP4.5 and RCP8.5. Dashed lines indicate the upper and deep ETP regions. Note the nonlinear color scale and that the Sea of Japan has been excluded so that these zonal means are more cleanly interpretable.

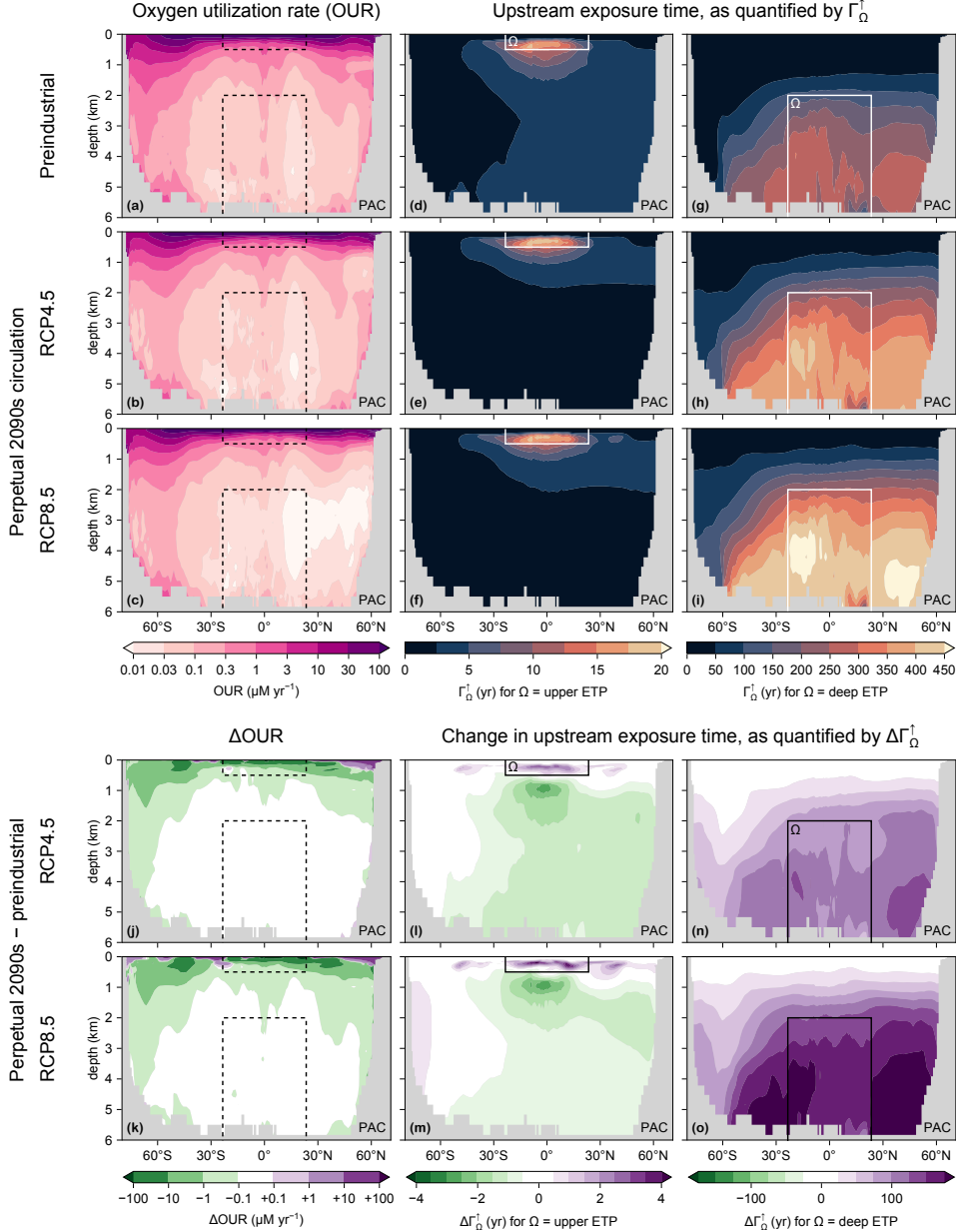


**Figure B2.** (a) Pacific zonal mean OUR for the preindustrial state. Dashed lines indicate the upper and deep ETP regions ( $\Omega$ 's). (b–c) As (a) for the perpetual-2090s states (RCP4.5 and RCP8.5). (d–f) As (a–c) for the upstream exposure time  $\Gamma_\Omega^\uparrow$  of the upper ETP (above 500 m; solid white line). (g–i) As (d–f) for the deep ETP (below 2000 m). (j–k) As (b–c) for  $\Delta\text{OUR}$ . (l,m,n,o) As (e,f,h,i) for  $\Delta\Gamma_\Omega^\uparrow$ . Note the nonlinear color scales and that the Sea of Japan has been excluded so that these zonal means are more cleanly interpretable.

the deep ETP, the circulation slowdown drives strong  $\Gamma_\Omega^\uparrow$  increases throughout the deep Pacific north of the Southern Ocean. By contrast, for the upper ETP,  $\Gamma_\Omega^\uparrow$  increases above

500 m, but decreases in the Pacific below the thermocline north of  $\sim 30^{\circ}\text{S}$ . These decreases are likely because the surface ocean becomes more isolated in our perpetual-2090s states (Pasquier et al., 2024), reducing the flow of mid-depth, low-latitude waters through the upper ETP on their way back to the surface. Conversely, slight increases in  $\Gamma_{\Omega}^{\uparrow}$  in the deep polar Southern Ocean for RCP8.5 are likely due to deep Southern Ocean waters preferentially upwelling at lower latitudes instead of being quickly mixed back to the Southern Ocean euphotic zone.

Changes in  $\text{O}_2^{\text{pre}}$  are driven by changes in euphotic  $\text{O}_2$  and by changes in ventilation patterns. Fig. B3 shows maps of the changes in euphotic-mean oxygen concentrations. Except at high latitudes, declines are widespread and attributable to warming-driven solubility reductions. Increases can be caused by decreased temperatures (e.g., in the North Atlantic cold blob) but the most intense increases occur near the Weddell and Ross Seas due to reduced vertical mixing, which allows for better air-sea oxygen equilibration as discussed in Section 3.2 of the main text. However, solubility changes are not the dominant driver of reduced interior  $\text{O}_2^{\text{pre}}$  concentrations.

Decreases in the  $\text{O}_2^{\text{pre}}$  inventory of an interior subvolume  $\Omega$  are dominantly driven by changes in ventilation patterns (Section 3.2), as quantified by the amount of the  $\Omega$  volume ventilated per unit area,  $\mathcal{V}_{\Omega}^{\downarrow}$ . Maps of  $\mathcal{V}_{\Omega}^{\downarrow}$  for  $\Omega$  being the upper and deep ETP are plotted in Fig. B4 for the preindustrial state, along with the changes for our perpetual-2090s states. The patterns of  $\mathcal{V}_{\Omega}^{\downarrow}$  strongly mirror those of  $\text{O}_2 \mathcal{V}_{\Omega}^{\downarrow}$  in Fig. 9 of the main text. While  $\sim 40\%$  of the upper ETP is ventilated from directly above, the remaining  $\sim 60\%$  is ventilated from distant regions, with subtropical and subpolar contributions in the Pacific, as well as contributions from the North Atlantic, the Ross Sea, and the Weddell Sea. By contrast, the bulk of the deep ETP is ventilated from distant regions, with only about 1% from directly above. In our perpetual-2090s states, the subpolar and Southern Ocean contributions generally decline in favor of subtropical and tropical contributions, effectively shifting the origin of preformed  $\text{O}_2$  equatorward where warmer waters hold less dissolved oxygen.

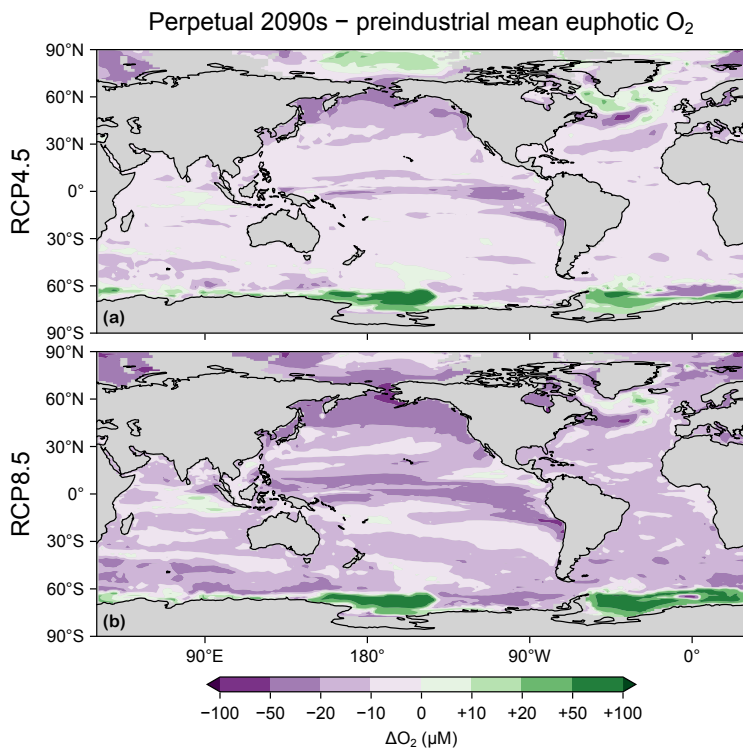


**Figure B3.** (a) Change in the euphotic-mean  $O_2$  between the preindustrial state and the perpetual-2090s state for the RCP4.5 scenario. (b) As (a) for RCP8.5. Note the nonlinear color scale.

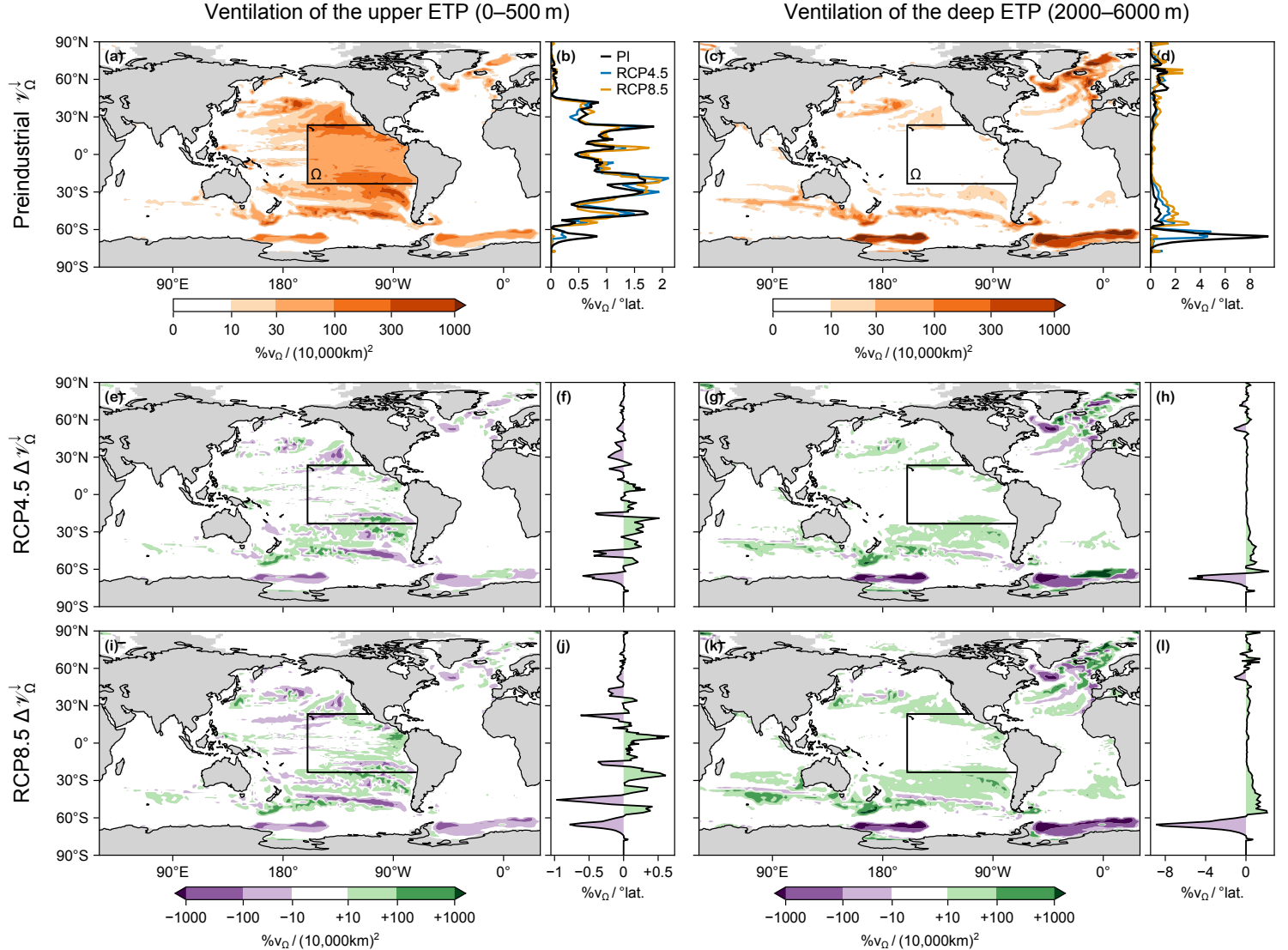


**Figure B4.** (a) Map and (b) zonal integral of the fractional  $\Omega$  volume ventilated from the surface for  $\Omega$  being the upper ETP (solid black contour), as quantified by  $\mathcal{V}_\Omega^\downarrow$ , in the preindustrial state. (c–d) As (a–b) for  $\Omega$  being the deep ETP. (e–h) As (a–d) for  $\Delta\mathcal{V}_\Omega^\downarrow$  in the RCP4.5 scenario. (i–l) As (e–h) in the RCP8.5 scenario. Note the nonlinear color scales.

928 **Appendix C Open Research**

929 The MATLAB and Julia code corresponding to this work will be made available  
 930 upon acceptance of this article. The figures were created in Julia (Bezanson et al., 2017)  
 931 with the Makie.jl plotting package (Danisch & Krumbiegel, 2021). The transport ma-  
 932 trices were built from the historical, RCP4.5, and RCP8.5 ACCESS1.3 CMIP5 model  
 933 runs available at <https://esgf.nci.org.au/projects/esgf-nci/>. This output also  
 934 includes temperature, salinity, photosynthetically available radiation (PAR), sea-ice, and  
 935 wind fields.

936 **Acknowledgments**

937 This work was supported by Australian Research Council grant DP210101650 (to  
 938 MH) and undertaken with the assistance of resources and services from the National Com-  
 939 putational Infrastructure (NCI), which is supported by the Australian Government. NLB  
 940 support for this project received grant funding from the Australian Government as part  
 941 of the Antarctic Science Collaboration Initiative program.

942 **References**

- 943 Arias, P., Bellouin, N., Coppola, E., Jones, R., Krinner, G., Marotzke, J., ... Zickfeld,  
 944 K. (2021). Technical summary [Book Section]. In V. Masson-Delmotte et  
 945 al. (Eds.), *Climate change 2021: The physical science basis. contribution of  
 946 working group i to the sixth assessment report of the intergovernmental panel  
 947 on climate change* (pp. 33–144). Cambridge, United Kingdom and New York,  
 948 NY, USA: Cambridge University Press. doi: 10.1017/9781009157896.002
- 949 Bao, Y., & Li, Y. (2016, December). Simulations of dissolved oxygen concentration  
 950 in CMIP5 Earth system models. *Acta Oceanologica Sinica*, 35(12), 28–37. doi:  
 951 10.1007/s13131-016-0959-x
- 952 Beman, J. M., & Carolan, M. T. (2013). Deoxygenation alters bacterial diversity  
 953 and community composition in the ocean's largest oxygen minimum zone. *Na-  
 954 ture Communications*, 4(1), 2705. doi: 10.1038/ncomms3705
- 955 Bezanson, J., Edelman, A., Karpinski, S., & Shah, V. B. (2017). Julia: A fresh ap-  
 956 proach to numerical computing. *SIAM Review*, 59(1), 65–98. doi: 10.1137/  
 957 141000671

- 958 Bi, D., Marsland, S. J., Uotila, P., O'Farrell, S., Fiedler, R. A. S., Sullivan, A., ...  
 959 Hirst, A. C. (2013). ACCESS-OM: the ocean and sea ice core of the ACCESS  
 960 coupled model. *Australian Meteorological and Oceanographic Journal*, 63,  
 961 213-232.
- 962 Bindoff, N. L., Cheung, W. W. L., Kairo, J. G., Arístegui, J., Guinder, V. A.,  
 963 Hallberg, R., ... Williamson, P. (2022). Changing Ocean, Marine Ecosys-  
 964 tems, and Dependent Communities. In *The Ocean and Cryosphere in a*  
 965 *Changing Climate: Special Report of the Intergovernmental Panel on Cli-*  
 966 *mate Change* (pp. 447–588). Cambridge: Cambridge University Press. doi:  
 967 10.1017/9781009157964.007
- 968 Bopp, L., Le Quéré, C., Heimann, M., Manning, A. C., & Monfray, P. (2002).  
 969 Climate-induced oceanic oxygen fluxes: Implications for the contempo-  
 970 rary carbon budget. *Global Biogeochemical Cycles*, 16(2), 6-1-6-13. doi:  
 971 10.1029/2001GB001445
- 972 Bopp, L., Resplandy, L., Orr, J. C., Doney, S. C., Dunne, J. P., Gehlen, M., ...  
 973 Vichi, M. (2013). Multiple stressors of ocean ecosystems in the 21st cen-  
 974 tury: Projections with CMIP5 models. *Biogeosciences*, 10(10), 6225–6245. doi:  
 975 10.5194/bg-10-6225-2013
- 976 Bopp, L., Resplandy, L., Untersee, A., Le Mezo, P., & Kageyama, M. (2017). Ocean  
 977 (de)oxygenation from the Last Glacial Maximum to the twenty-first cen-  
 978 tury: Insights from Earth System models. *Philosophical Transactions of the*  
 979 *Royal Society A: Mathematical, Physical and Engineering Sciences*, 375(2102),  
 980 20160323. doi: 10.1098/rsta.2016.0323
- 981 Brandt, P., Bange, H. W., Banyte, D., Dengler, M., Didwischus, S.-H., Fischer, T.,  
 982 ... Visbeck, M. (2015). On the role of circulation and mixing in the ventilation  
 983 of oxygen minimum zones with a focus on the eastern tropical North Atlantic.  
 984 *Biogeosciences*, 12(2), 489–512. doi: 10.5194/bg-12-489-2015
- 985 Breitburg, D., Levin, L. A., Oschlies, A., Grégoire, M., Chavez, F. P., Conley, D. J.,  
 986 ... Zhang, J. (2018). Declining oxygen in the global ocean and coastal waters.  
 987 *Science*, 359(6371), eaam7240. doi: 10.1126/science.aam7240
- 988 Broecker, W. S., & Peng, T.-H. (1982). Tracers in the Sea. *Lamont-Doherty Geolog-*  
 989 *ical Observatory, Columbia University Palisades, New York*, 24(3), b1-b2. doi:  
 990 10.1017/S0033822200005221

- 991 Buchanan, P. J., & Tagliabue, A. (2021). The Regional Importance of Oxygen De-  
 992 mand and Supply for Historical Ocean Oxygen Trends. *Geophysical Research*  
 993 *Letters*, 48(20), e2021GL094797. doi: 10.1029/2021GL094797
- 994 Busecke, J. J. M., Resplandy, L., Ditkovsky, S. J., & John, J. G. (2022). Diverging  
 995 Fates of the Pacific Ocean Oxygen Minimum Zone and Its Core in a Warming  
 996 World. *AGU Advances*, 3(6), e2021AV000470. doi: 10.1029/2021AV000470
- 997 Chamberlain, M. A., Matear, R. J., Holzer, M., Bi, D., & Marsland, S. J. (2019).  
 998 Transport matrices from standard ocean-model output and quantifying cir-  
 999 culation response to climate change. *Ocean Modelling*, 135, 1-13. doi:  
 1000 10.1016/j.ocemod.2019.01.005
- 1001 Chen, J.-J., Swart, N. C., Beadling, R., Cheng, X., Hattermann, T., Jüling, A., ...  
 1002 Thomas, M. (2023). Reduced Deep Convection and Bottom Water Formation  
 1003 Due To Antarctic Meltwater in a Multi-Model Ensemble. *Geophysical Research*  
 1004 *Letters*, 50(24), e2023GL106492. doi: 10.1029/2023GL106492
- 1005 Cheng, L., von Schuckmann, K., Abraham, J. P., Trenberth, K. E., Mann, M. E.,  
 1006 Zanna, L., ... Lin, X. (2022). Past and future ocean warming. *Nature Reviews*  
 1007 *Earth & Environment*, 3(11), 776–794. doi: 10.1038/s43017-022-00345-1
- 1008 Cliff, E., Khatiwala, S., & Schmittner, A. (2021). Glacial deep ocean deoxygena-  
 1009 tion driven by biologically mediated air-sea disequilibrium. *Nature Geoscience*,  
 1010 14(1), 43–50. doi: 10.1038/s41561-020-00667-z
- 1011 Couespe, D., Lévy, M., & Bopp, L. (2019). Major Contribution of Reduced  
 1012 Upper Ocean Oxygen Mixing to Global Ocean Deoxygenation in an Earth  
 1013 System Model. *Geophysical Research Letters*, 46(21), 12239–12249. doi:  
 1014 10.1029/2019GL084162
- 1015 Danisch, S., & Krumbiegel, J. (2021). Makie.jl: Flexible high-performance data vi-  
 1016 sualization for Julia. *Journal of Open Source Software*, 6(65), 3349. doi: 10  
 1017 .21105/joss.03349
- 1018 de Boyer Montégut, C., Madec, G., Fischer, A. S., Lazar, A., & Iudicone, D. (2004).  
 1019 Mixed layer depth over the global ocean: An examination of profile data and a  
 1020 profile-based climatology. *Journal of Geophysical Research: Oceans*, 109(C12).  
 1021 doi: 10.1029/2004JC002378
- 1022 de Lavergne, C., Palter, J. B., Galbraith, E. D., Bernardello, R., & Marinov, I.  
 1023 (2014). Cessation of deep convection in the open Southern Ocean under an-

- 1024 thropogenic climate change. *Nature Climate Change*, 4(4), 278–282. doi:  
1025 10.1038/nclimate2132

1026 Deutsch, C., Emerson, S., & Thompson, L. (2006). Physical-biological interactions  
1027 in North Pacific oxygen variability. *Journal of Geophysical Research: Oceans*,  
1028 111(C9). doi: 10.1029/2005JC003179

1029 Deutsch, C., Ferrel, A., Seibel, B., Pörtner, H.-O., & Huey, R. B. (2015). Climate  
1030 change tightens a metabolic constraint on marine habitats. *Science*, 348(6239),  
1031 1132–1135. doi: 10.1126/science.aaa1605

1032 Deutsch, C., Penn, J. L., & Lucey, N. (2024). Climate, Oxygen, and the Future of  
1033 Marine Biodiversity. *Annual Review of Marine Science*, 16(1), null. doi: 10.  
1034 .1146/annurev-marine-040323-095231

1035 DeVries, T., & Deutsch, C. (2014). Large-scale variations in the stoichiometry of ma-  
1036 rine organic matter respiration. *Nature Geoscience*, 7, 890–894. doi: 10.1038/  
1037 NGEO2300

1038 Diaz, R. J., & Rosenberg, R. (2008). Spreading Dead Zones and Consequences  
1039 for Marine Ecosystems. *Science*, 321(5891), 926–929. doi: 10.1126/science  
1040 .1156401

1041 Doney, S. C., & Bullister, J. L. (1992). A chlorofluorocarbon section in the east-  
1042 ern North Atlantic. *Deep Sea Research Part A. Oceanographic Research Pa-*  
1043 *pers*, 39(11), 1857–1883. doi: 10.1016/0198-0149(92)90003-C

1044 Duteil, O., Koeve, W., Oschlies, A., Bianchi, D., Galbraith, E., Kriest, I., & Matear,  
1045 R. (2013). A novel estimate of ocean oxygen utilisation points to a reduced  
1046 rate of respiration in the ocean interior. *Biogeosciences*, 10(11), 7723–7738.  
1047 doi: 10.5194/bg-10-7723-2013

1048 Earle, S. A., Wright, D. J., Joye, S., Laffoley, D., Baxter, J., Safina, C., & Elkus, P.  
1049 (2018, March). Ocean deoxygenation: Time for action. *Science*, 359(6383),  
1050 1475–1476. doi: 10.1126/science.aat0167

1051 Eggleston, S., & Galbraith, E. D. (2018). The devil's in the disequilibrium: Multi-  
1052 component analysis of dissolved carbon and oxygen changes under a broad  
1053 range of forcings in a general circulation model. *Biogeosciences*, 15(12),  
1054 3761–3777. doi: 10.5194/bg-15-3761-2018

1055 Ekau, W., Auel, H., Pörtner, H.-O., & Gilbert, D. (2010). Impacts of hy-  
1056 poxia on the structure and processes in pelagic communities (zooplank-

- ton, macro-invertebrates and fish). *Biogeosciences*, 7(5), 1669–1699. doi: 10.5194/bg-7-1669-2010
- Espinoza-Morriberón, D., Echevin, V., Gutiérrez, D., Tam, J., Graco, M., Ledesma, J., & Colas, F. (2021). Evidences and drivers of ocean deoxygenation off Peru over recent past decades. *Scientific Reports*, 11(1), 20292. doi: 10.1038/s41598-021-99876-8
- Falkowski, P. G., & Godfrey, L. V. (2008). Electrons, life and the evolution of Earth's oxygen cycle. *Philosophical Transactions of the Royal Society B: Biological Sciences*, 363(1504), 2705–2716. doi: 10.1098/rstb.2008.0054
- Feely, R. A., Sabine, C. L., Schlitzer, R., Bullister, J. L., Mecking, S., & Greeley, D. (2004). Oxygen Utilization and Organic Carbon Remineralization in the Upper Water Column of the Pacific Ocean. *Journal of Oceanography*, 60(1), 45–52. doi: 10.1023/B:JOCE.0000038317.01279.aa
- Franco, A. C., Kim, H., Frenzel, H., Deutsch, C., Ianson, D., Sumaila, U. R., & Tortell, P. D. (2022). Impact of warming and deoxygenation on the habitat distribution of Pacific halibut in the Northeast Pacific. *Fisheries Oceanography*, 31(6), 601–614. doi: 10.1111/fog.12610
- Frölicher, T. L., Aschwanden, M. T., Gruber, N., Jaccard, S. L., Dunne, J. P., & Paynter, D. (2020). Contrasting Upper and Deep Ocean Oxygen Response to Protracted Global Warming. *Global Biogeochemical Cycles*, 34(8), e2020GB006601. doi: 10.1029/2020GB006601
- Fu, W., Bardin, A., & Primeau, F. W. (2018). Tracing ventilation source of tropical pacific oxygen minimum zones with an adjoint global ocean transport model. *Deep Sea Research Part I: Oceanographic Research Papers*, 139, 95–103. doi: 10.1016/j.dsr.2018.07.017
- Gallo, N. D., & Levin, L. A. (2016). Chapter Three - Fish Ecology and Evolution in the World's Oxygen Minimum Zones and Implications of Ocean Deoxygenation. In B. E. Curry (Ed.), *Advances in Marine Biology* (Vol. 74, pp. 117–198). Academic Press. doi: 10.1016/bs.amb.2016.04.001
- Gnanadesikan, A., Dunne, J. P., & John, J. (2012). Understanding why the volume of suboxic waters does not increase over centuries of global warming in an Earth System Model. *Biogeosciences*, 9(3), 1159–1172. doi: 10.5194/bg-9-1159-2012

- 1090 Graco, M. I., Purca, S., Dewitte, B., Castro, C. G., Morón, O., Ledesma, J., ...  
 1091 Gutiérrez, D. (2017). The OMZ and nutrient features as a signature of in-  
 1092 terannual and low-frequency variability in the Peruvian upwelling system.  
 1093 *Biogeosciences*, 14(20), 4601–4617. doi: 10.5194/bg-14-4601-2017
- 1094 Gunn, K. L., Rintoul, S. R., England, M. H., & Bowen, M. M. (2023). Recent re-  
 1095 duced abyssal overturning and ventilation in the Australian Antarctic Basin.  
 1096 *Nature Climate Change*, 13(6), 537–544. doi: 10.1038/s41558-023-01667-8
- 1097 Helm, K. P., Bindoff, N. L., & Church, J. A. (2011). Observed decreases in oxy-  
 1098 gen content of the global ocean. *Geophysical Research Letters*, 38(23). doi: 10  
 1099 .1029/2011GL049513
- 1100 Heuzé, C., Heywood, K. J., Stevens, D. P., & Ridley, J. K. (2013). Southern Ocean  
 1101 bottom water characteristics in CMIP5 models. *Geophysical Research Letters*,  
 1102 40(7), 1409–1414. doi: 10.1002/grl.50287
- 1103 Heuzé, C., Heywood, K. J., Stevens, D. P., & Ridley, J. K. (2015). Changes in  
 1104 Global Ocean Bottom Properties and Volume Transports in CMIP5 Models  
 1105 under Climate Change Scenarios. *Journal of Climate*, 28(8), 2917–2944. doi:  
 1106 10.1175/JCLI-D-14-00381.1
- 1107 Hofmann, A. F., Peltzer, E. T., Walz, P. M., & Brewer, P. G. (2011). Hypoxia by  
 1108 degrees: Establishing definitions for a changing ocean. *Deep Sea Research Part*  
 1109 *I: Oceanographic Research Papers*, 58(12), 1212–1226. doi: 10.1016/j.dsr.2011  
 1110 .09.004
- 1111 Holzer, M. (2022). The fate of oxygen in the ocean and its sensitivity to lo-  
 1112 cal changes in biological production. *Journal of Geophysical Research:*  
 1113 *Oceans*, 127(8), e2022JC018802. (e2022JC018802 2022JC018802) doi:  
 1114 10.1029/2022JC018802
- 1115 Holzer, M., Chamberlain, M. A., & Matear, R. J. (2020). Climate-driven changes  
 1116 in the ocean's ventilation pathways and time scales diagnosed from transport  
 1117 matrices. *Journal of Geophysical Research: Oceans*, 125(10), e2020JC016414.  
 1118 (e2020JC016414 10.1029/2020JC016414) doi: 10.1029/2020JC016414
- 1119 Holzer, M., DeVries, T., & de Lavergne, C. (2021). Diffusion controls the ventilation  
 1120 of a Pacific Shadow Zone above abyssal overturning. *Nature Communications*,  
 1121 12(1), 4348. doi: 10.1038/s41467-021-24648-x
- 1122 Holzer, M., & Hall, T. M. (2000). Transit-Time and Tracer-Age Distributions in

- 1123                   Geophysical Flows.     *Journal of the Atmospheric Sciences*, 57(21), 3539–3558.  
 1124                   doi: 10.1175/1520-0469(2000)057<3539:TTATAD>2.0.CO;2
- 1125                   Ito, T. (2022). Optimal interpolation of global dissolved oxygen: 1965–2015. *Geo-*  
 1126                   *science Data Journal*, 9(1), 167–176. doi: 10.1002/gdj3.130
- 1127                   Ito, T., Follows, M. J., & Boyle, E. A. (2004). Is AOU a good measure of respi-  
 1128                   ration in the oceans? *Geophysical Research Letters*, 31(17). doi: 10.1029/  
 1129                   2004GL020900
- 1130                   Ito, T., Garcia, H. E., Wang, Z., Minobe, S., Long, M. C., Cebrian, J., ... Deutsch,  
 1131                   C. A. (2024). Underestimation of multi-decadal global O<sub>2</sub> loss due to  
 1132                   an optimal interpolation method. *Biogeosciences*, 21(3), 747–759. doi:  
 1133                   10.5194/bg-21-747-2024
- 1134                   Ito, T., Minobe, S., Long, M. C., & Deutsch, C. (2017). Upper ocean O<sub>2</sub> trends:  
 1135                   1958–2015. *Geophysical Research Letters*, 44(9), 4214–4223. doi: 10.1002/  
 1136                   2017GL073613
- 1137                   Ito, T., Takano, Y., Deutsch, C., & Long, M. C. (2022). Sensitivity of Global  
 1138                   Ocean Deoxygenation to Vertical and Isopycnal Mixing in an Ocean Biogeo-  
 1139                   chemistry Model. *Global Biogeochemical Cycles*, 36(4), e2021GB007151. doi:  
 1140                   10.1029/2021GB007151
- 1141                   Jin, X., Najjar, R. G., Louanchi, F., & Doney, S. C. (2007). A modeling study of the  
 1142                   seasonal oxygen budget of the global ocean. *Journal of Geophysical Research:*  
 1143                   *Oceans*, 112(C5). doi: 10.1029/2006JC003731
- 1144                   Keeling, R. F., & Garcia, H. E. (2002). The change in oceanic O<sub>2</sub> inventory associ-  
 1145                   ated with recent global warming. *Proceedings of the National Academy of Sci-*  
 1146                   *ences*, 99(12), 7848–7853. doi: 10.1073/pnas.122154899
- 1147                   Keeling, R. F., Körtzinger, A., & Gruber, N. (2010). Ocean Deoxygenation in a  
 1148                   Warming World. *Annual Review of Marine Science*, 2(1), 199–229. doi: 10  
 1149                   .1146/annurev.marine.010908.163855
- 1150                   Koeve, W., & Kähler, P. (2016). Oxygen utilization rate (OUR) underestimates  
 1151                   ocean respiration: A model study. *Global Biogeochemical Cycles*, 30(8),  
 1152                   1166–1182. doi: 10.1002/2015GB005354
- 1153                   Kwiatkowski, L., Torres, O., Bopp, L., Aumont, O., Chamberlain, M., Christian,  
 1154                   J. R., ... Ziehn, T. (2020). Twenty-first century ocean warming, acidifica-  
 1155                   tion, deoxygenation, and upper-ocean nutrient and primary production decline

- from CMIP6 model projections. *Biogeosciences*, 17(13), 3439–3470. doi: 10.5194/bg-17-3439-2020
- Laffoley, D., & Baxter, J. M. (2019). *Ocean deoxygenation: Everyone's problem: Causes, impacts, consequences and solutions: Summary for Policy Makers* (Report). Gland: International Union for Conservation of Nature (IUCN). doi: 10.2305/IUCN.CH.2019.14.en
- Lauvset, S. K., Key, R. M., Olsen, A., van Heuven, S., Velo, A., Lin, X., ... Wa-telet, S. (2016). A new global interior ocean mapped climatology: The  $1 \times 1$  GLODAP version 2. *Earth System Science Data*, 8(2), 325–340. doi: 10.5194/essd-8-325-2016
- Levin, L. A. (2018). Manifestation, Drivers, and Emergence of Open Ocean De-oxygenation. *Annual Review of Marine Science*, 10, 229–260. doi: 10.1146/annurev-marine-121916-063359
- Li, Q., England, M. H., Hogg, A. M., Rintoul, S. R., & Morrison, A. K. (2023). Abyssal ocean overturning slowdown and warming driven by Antarctic meltwater. *Nature*, 615(7954), 841–847. doi: 10.1038/s41586-023-05762-w
- Long, M. C., Ito, T., & Deutsch, C. (2019). Oxygen projections for the future. In *Ocean deoxygenation: Everyone's problem — causes, impacts, consequences and solutions* (pp. 171–211). Gland, Switzerland: IUCN.
- Marsland, S., Bi, D., Uotila, P., Fiedler, R., Griffies, S., Lorbacher, K., ... Hirst, A. (2013). Configuration and spin-up of ACCESS-CM2, the new generation Australian Community Climate and Earth System Simulator Coupled Model. *Australian Meteorological and Oceanographic Journal*, 63, 101–119. doi: 10.22499/2.6301.007
- Matear, R. J., & Hirst, A. C. (2003). Long-term changes in dissolved oxygen concentrations in the ocean caused by protracted global warming. *Global Biogeochemical Cycles*, 17(4). doi: 10.1029/2002GB001997
- Matear, R. J., Hirst, A. C., & McNeil, B. I. (2000). Changes in dissolved oxygen in the Southern Ocean with climate change. *Geochemistry, Geophysics, Geosystems*, 1(11). doi: 10.1029/2000GC000086
- McCormick, L. R., & Levin, L. A. (2017). Physiological and ecological implications of ocean deoxygenation for vision in marine organisms. *Philosophical Transactions of the Royal Society A: Mathematical, Physical and Engineering Sciences*,

- 1189                   375(2102), 20160322. doi: 10.1098/rsta.2016.0322
- 1190                   Meinshausen, M., Nicholls, Z. R. J., Lewis, J., Gidden, M. J., Vogel, E., Freund, M.,  
 1191                   ... Wang, R. H. J. (2020). The shared socio-economic pathway (ssp) green-  
 1192                   house gas concentrations and their extensions to 2500. *Geoscientific Model  
 Development*, 13(8), 3571–3605. doi: 10.5194/gmd-13-3571-2020
- 1193                   Meinshausen, M., Smith, S. J., Calvin, K., Daniel, J. S., Kainuma, M. L. T., Lamar-  
 1194                   que, J.-F., ... van Vuuren, D. P. (2011). The RCP greenhouse gas concentra-  
 1195                   tions and their extensions from 1765 to 2300. *Climatic Change*, 109(1), 213.  
 1196                   doi: 10.1007/s10584-011-0156-z
- 1197                   Mongwe, P., Long, M., Ito, T., Deutsch, C., & Santana-Falcón, Y. (under review).  
 1198                   Climatic Controls on Metabolic Constraints in the Ocean. *EGUsphere*, 1–29.  
 1199                   doi: 10.5194/egusphere-2023-2822
- 1200                   Moore, J. K., Fu, W., Primeau, F. W., Britten, G. L., Lindsay, K., Long, M.,  
 1201                   ... Randerson, J. T. (2018). Sustained climate warming drives declin-  
 1202                   ing marine biological productivity. *Science*, 359(6380), 1139-1143. doi:  
 1203                   10.1126/science.aa06379
- 1204                   Morée, A. L., Clarke, T. M., Cheung, W. W. L., & Frölicher, T. L. (2023). Impact of  
 1205                   deoxygenation and warming on global marine species in the 21st century. *Bio-  
 1206                   geosciences*, 20(12), 2425–2454. doi: 10.5194/bg-20-2425-2023
- 1207                   Oschlies, A. (2021). A committed fourfold increase in ocean oxygen loss. *Nature  
 Communications*, 12(1), 2307. doi: 10.1038/s41467-021-22584-4
- 1208                   Oschlies, A., Brandt, P., Stramma, L., & Schmidtko, S. (2018). Drivers and mech-  
 1209                   anisms of ocean deoxygenation. *Nature Geoscience*, 11(7), 467–473. doi: 10  
 1210                   .1038/s41561-018-0152-2
- 1211                   Oschlies, A., Koeve, W., Landolfi, A., & Kähler, P. (2019). Loss of fixed nitro-  
 1212                   gen causes net oxygen gain in a warmer future ocean. *Nature Communications*,  
 1213                   10(1), 2805. doi: 10.1038/s41467-019-10813-w
- 1214                   Palter, J. B., & Trossman, D. S. (2018). The Sensitivity of Future Ocean Oxygen to  
 1215                   Changes in Ocean Circulation. *Global Biogeochemical Cycles*, 32(5), 738–751.  
 1216                   doi: 10.1002/2017GB005777
- 1217                   Pascal, L., Cool, J., Archambault, P., Calosi, P., Cuenca, A. L. R., Mucci, A. O.,  
 1218                   & Chaillou, G. (2023). Ocean deoxygenation caused non-linear responses in  
 1219                   the structure and functioning of benthic ecosystems. *Global Change Biology*,

- 1222            *n/a(n/a)*, e16994. doi: 10.1111/gcb.16994
- 1223     Pasquier, B., Holzer, M., & Chamberlain, M. A. (2024). The biological and pre-  
1224        formed carbon pumps in perpetually slower and warmer oceans. *Biogeo-  
1225        sciences*, 21(14), 3373–3400. doi: 10.5194/bg-21-3373-2024
- 1226     Pasquier, B., Holzer, M., Chamberlain, M. A., Matear, R. J., Bindoff, N. L., &  
1227        Primeau, F. W. (2023). Optimal parameters for the ocean's nutrient,  
1228        carbon, and oxygen cycles compensate for circulation biases but replumb  
1229        the biological pump. *Biogeosciences (Online)*, 20(14), 2985–3009. doi:  
1230        10.5194/bg-20-2985-2023
- 1231     Pitcher, G. C., Aguirre-Velarde, A., Breitburg, D., Cardich, J., Carstensen, J.,  
1232        Conley, D. J., ... Zhu, ZY. (2021). System controls of coastal and open  
1233        ocean oxygen depletion. *Progress in Oceanography*, 197, 102613. doi:  
1234        10.1016/j.pocean.2021.102613
- 1235     Plattner, G.-K., Joos, F., Stocker, T. F., & Marchal, O. (2001). Feedback mecha-  
1236        nisms and sensitivities of ocean carbon uptake under global warming. *Tellus B:  
1237        Chemical and Physical Meteorology*, 53(5), 564–592. doi: 10.3402/tellusb.v53i5  
1238        .16637
- 1239     Primeau, F. W. (2005). Characterizing transport between the surface mixed  
1240        layer and the ocean interior with a forward and adjoint global ocean trans-  
1241        port model. *Journal of Physical Oceanography*, 35(4), 545–564. doi:  
1242        10.1175/JPO2699.1
- 1243     Purich, A., & England, M. H. (2023). Projected Impacts of Antarctic Meltwa-  
1244        ter Anomalies over the Twenty-First Century. *Journal of Climate*, 36(8),  
1245        2703–2719. doi: 10.1175/JCLI-D-22-0457.1
- 1246     Purich, A., England, M. H., Cai, W., Sullivan, A., & Durack, P. J. (2018). Impacts  
1247        of Broad-Scale Surface Freshening of the Southern Ocean in a Coupled Climate  
1248        Model. *Journal of Climate*, 31(7), 2613–2632. doi: 10.1175/JCLI-D-17-0092.1
- 1249     Riahi, K., van Vuuren, D. P., Kriegler, E., Edmonds, J., O'Neill, B. C., Fujimori, S.,  
1250        ... Tavoni, M. (2017). The shared socioeconomic pathways and their energy,  
1251        land use, and greenhouse gas emissions implications: An overview. *Global  
1252        Environmental Change*, 42, 153–168. doi: 10.1016/j.gloenvcha.2016.05.009
- 1253     Roach, C. J., & Bindoff, N. L. (2023). Developing a New Oxygen Atlas of the  
1254        World's Oceans Using Data Interpolating Variational Analysis. *Jour-*

- 1255 *nal of Atmospheric and Oceanic Technology*, 40(11), 1475–1491. doi:  
1256 10.1175/JTECH-D-23-0007.1

1257 Rogers, A. D. (2000). The role of the oceanic oxygen minima in generating biodiver-  
1258 sity in the deep sea. *Deep Sea Research Part II: Topical Studies in Oceanogra-*  
1259 *phy*, 47(1), 119–148. doi: 10.1016/S0967-0645(99)00107-1

1260 Russell, J. L., & Dickson, A. G. (2003). Variability in oxygen and nutrients in South  
1261 Pacific Antarctic Intermediate Water. *Global Biogeochemical Cycles*, 17(2).  
1262 doi: 10.1029/2000GB001317

1263 Sarmiento, J. L., Herbert, T. D., & Toggweiler, J. R. (1988). Causes of anoxia in  
1264 the world ocean. *Global Biogeochemical Cycles*, 2(2), 115–128. doi: 10.1029/  
1265 GB002i002p00115

1266 Sato, K. N., Levin, L. A., & Schiff, K. (2017). Habitat compression and expansion of  
1267 sea urchins in response to changing climate conditions on the California conti-  
1268 nental shelf and slope (1994–2013). *Deep Sea Research Part II: Topical Studies*  
1269 *in Oceanography*, 137, 377–389. doi: 10.1016/j.dsr2.2016.08.012

1270 Schmidtko, S., Stramma, L., & Visbeck, M. (2017). Decline in global oceanic oxy-  
1271 gen content during the past five decades. *Nature*, 542(7641), 335–339. doi: 10.  
1272 .1038/nature21399

1273 Schmittner, A., Oschlies, A., Matthews, H. D., & Galbraith, E. D. (2008). Future  
1274 changes in climate, ocean circulation, ecosystems, and biogeochemical cycling  
1275 simulated for a business-as-usual co2 emission scenario until year 4000 ad.  
1276 *Global Biogeochemical Cycles*, 22(1). doi: 10.1029/2007GB002953

1277 Seibel, B. A. (2011). Critical oxygen levels and metabolic suppression in oceanic  
1278 oxygen minimum zones. *Journal of Experimental Biology*, 214(2), 326–336. doi:  
1279 10.1242/jeb.049171

1280 Shaffer, G., Olsen, S. M., & Pedersen, J. O. P. (2009). Long-term ocean oxygen de-  
1281 pletion in response to carbon dioxide emissions from fossil fuels. *Nature Geo-*  
1282 *science*, 2(2), 105–109. doi: 10.1038/ngeo420

1283 Sonnerup, R. E., Mecking, S., & Bullister, J. L. (2013). Transit time distributions  
1284 and oxygen utilization rates in the Northeast Pacific Ocean from chlorofluo-  
1285 rocarbons and sulfur hexafluoride. *Deep Sea Research Part I: Oceanographic*  
1286 *Research Papers*, 72, 61–71. doi: 10.1016/j.dsr.2012.10.013

1287 Sonnerup, R. E., Mecking, S., Bullister, J. L., & Warner, M. J. (2015). Transit time

- 1288 distributions and oxygen utilization rates from chlorofluorocarbons and sulfur  
 1289 hexafluoride in the Southeast Pacific Ocean. *Journal of Geophysical Research: Oceans*, 120(5), 3761–3776. doi: 10.1002/2015JC010781
- 1290
- 1291 Srokosz, M. A., & Bryden, H. L. (2015). Observing the Atlantic Meridional Over-  
 1292 turning Circulation yields a decade of inevitable surprises. *Science*, 348(6241),  
 1293 1255575. doi: 10.1126/science.1255575
- 1294
- 1295 Stramma, L., Prince, E. D., Schmidtko, S., Luo, J., Hoolihan, J. P., Visbeck, M., ...  
 1296 Körtzinger, A. (2012). Expansion of oxygen minimum zones may reduce avail-  
 1297 able habitat for tropical pelagic fishes. *Nature Climate Change*, 2(1), 33–37.  
 1298 doi: 10.1038/nclimate1304
- 1299
- 1300 Takano, Y., Ilyina, T., Tjiputra, J., Eddebbar, Y. A., Berthet, S., Bopp, L., ... Yool,  
 1301 A. (2023). Simulations of ocean deoxygenation in the historical era: Insights  
 1302 from forced and coupled models. *Frontiers in Marine Science*, 10.
- 1303
- 1304 Thomas, J. L., Waugh, D. W., & Gnanadesikan, A. (2020). Relationship between  
 1305 Age and Oxygen along Line W in the Northwest Atlantic Ocean. *Ocean Sci-  
 1306 ence Journal*, 55(2), 203–217. doi: 10.1007/s12601-020-0019-5
- 1307
- 1308 Vaquer-Sunyer, R., & Duarte, C. M. (2008). Thresholds of hypoxia for marine  
 1309 biodiversity. *Proceedings of the National Academy of Sciences*, 105(40),  
 1310 15452–15457. doi: 10.1073/pnas.0803833105
- 1311
- 1312 Wanninkhof, R. (2014). Relationship between wind speed and gas exchange over the  
 1313 ocean revisited. *Limnology and Oceanography: Methods*, 12(6), 351–362. doi:  
 1314 10.4319/lom.2014.12.351
- 1315
- 1316 Warner, M. J., Bullister, J. L., Wisegarver, D. P., Gammon, R. H., & Weiss, R. F.  
 1317 (1996). Basin-wide distributions of chlorofluorocarbons CFC-11 and CFC-12  
 1318 in the North Pacific: 1985–1989. *Journal of Geophysical Research: Oceans*,  
 1319 101(C9), 20525–20542. doi: 10.1029/96JC01849
- 1320
- 1321 Whitney, F. A., Freeland, H. J., & Robert, M. (2007). Persistently declining oxy-  
 1322 gen levels in the interior waters of the eastern subarctic Pacific. *Progress in  
 1323 Oceanography*, 75(2), 179–199. doi: 10.1016/j.pocean.2007.08.007
- 1324
- 1325 Wishner, K. F., Seibel, B. A., Roman, C., Deutsch, C., Outram, D., Shaw, C. T.,  
 1326 ... Riley, S. (2018). Ocean deoxygenation and zooplankton: Very small  
 1327 oxygen differences matter. *Science Advances*, 4(12), eaau5180. doi:  
 1328 10.1126/sciadv.aau5180

- 1321 Wyrki, K. (1962). The oxygen minima in relation to ocean circulation. *Deep*  
1322 *Sea Research and Oceanographic Abstracts*, 9(1), 11–23. doi: 10.1016/  
1323 0011-7471(62)90243-7
- 1324 Zheng, Y., Schlosser, P., Swift, J. H., & Jones, E. P. (1997). Oxygen utilization rates  
1325 in the Nansen Basin, Arctic Ocean: Implications for new production. *Deep Sea*  
1326 *Research Part I: Oceanographic Research Papers*, 44(12), 1923–1943. doi: 10  
1327 .1016/S0967-0637(97)00046-0